

A Matrix-Free Implicit Discontinuous Galerkin Method for Large Eddy Simulation of Transonic Buffet at High Reynolds Number on Graphics Processors

Ngoc Cuong Nguyen*, Sebastien Terrana†, and Jaime Peraire‡

Department of Aeronautics and Astronautics, Massachusetts Institute of Technology, Cambridge, MA, 02139

We present a wall-resolved implicit large eddy simulation (WRILES) of transonic buffet over the OAT15A supercritical airfoil at Mach number 0.73, angle of attack 3.5° and Reynolds number 3×10^6 . The simulation is performed using a high-order discontinuous Galerkin (DG) method and a diagonally implicit Runge-Kutta (DIRK) scheme on graphics processor units (GPUs). The WRILES method successfully predicts the buffet onset, the buffet frequency, and turbulence statistics owing to the high-order DG discretization and an efficient mesh refinement for the laminar and turbulent boundary layers. Various phenomena are captured, such as periodical low-frequency oscillations of shock wave in the streamwise direction, strong shear layer detached from the shock wave due to shock wave boundary layer interaction (SWBLI) and small scale structures broken down by the shear layer instability in the transition region, and shock-induced flow separation. The pressure coefficient, the root mean square (RMS) of the fluctuating pressure and the streamwise range of the shock wave oscillation agree well with the available experimental data. The results suggest that the proposed LES method can accurately predict the onset of turbulence and buffet phenomena at high Reynolds numbers without a subgrid scale model or a wall model.

I. Introduction

Transonic flows over an airfoil result in complex interactions between shock waves and viscous boundary layers. A particularly interesting phenomenon concerning modern supercritical airfoils is *transonic buffet*, whereby the flow separation induces a large-scale self-sustained motion of the shock over the surface of the airfoil. Transonic buffet can cause large-scale lift oscillations and structural vibrations that limit an aircraft's flight envelope. While the shock buffet phenomenon has been widely studied since it was first observed by Hilton and Fowler [1] in the post-war period, there is still no consensus on the exact mechanism governing the buffet dynamics (see reviews [2] and [3]). Therefore, new

*Principal Research Scientist, Department of Aeronautics and Astronautics, Massachusetts Institute of Technology, Cambridge, MA, 02139. Email: cuongng@mit.edu. Senior AIAA member.

†Postdoctoral Associate, Department of Aeronautics and Astronautics, Massachusetts Institute of Technology, Cambridge, MA, 02139. Email: terrana@mit.edu.

‡Professor, Department of Aeronautics and Astronautics, Massachusetts Institute of Technology, Cambridge, MA, 02139. Email: peraire@mit.edu. AIAA Fellow.

experimental and numerical studies are still desirable to achieve a better understanding of the phenomenon.

Among the experimental investigations of transonic buffet, the test campaign organized by ONERA on the OAT15A airfoil produced a variety of high-quality pressure and velocity measurements suitable for comparisons with numerical studies. The OAT15A airfoil was investigated experimentally by Jacquin et al. [4] at a freestream Mach number 0.73 and a chord-based Reynolds number 3×10^6 . The OAT15A is a supercritical wing section with a thickness-to-chord ratio of 12.3%, a chord of 0.23 m, and a blunt trailing edge measuring 0.005c. The airfoil model was tripped on both sides at $x/c = 0.07$ from the leading edge to trigger transition to turbulence at that location. The trip was 3 mm wide, with 0.089 mm grains on the lower side and 0.102 mm on the upper side. In the experiment, a periodic self-sustained shock-wave motion with the frequency of 69 Hz was observed over the top surface of the airfoil between $x/c = 0.35$ (most upstream shock position) and $x/c = 0.65$ (most downstream shock position) when the airfoil was kept at 3.5° angle of attack. The flow separates from the foot of the shock as the shock moves upward its most upstream position and reattaches as the shock moves downward its most downstream position.

The numerical prediction of transonic buffet is challenging due to the co-existence of multiple physical phenomena such as turbulent structures in the thin turbulent boundary layer (TBL) at high Reynolds number, unsteady shock wave, shock-induced separation, acoustic wave generation and propagation, and structural vibrations. Numerical tools for predicting transonic buffet rely mostly on turbulence models including Reynolds–Averaged Navier–Stokes (RANS), URANS, and DES. RANS is not capable of accurately predicting transonic buffet because it cannot capture the periodic motion of the shock. In the numerical simulations of transonic buffet, turbulence models have an enormous influence on the prediction accuracy of the buffet onset. For instance, The study of Thiery and Coustols [5] showed that the BSL and SA models yielded a steady solution, while the KKL and SST models produced periodic shock oscillations. Detached-eddy simulation (DES) is a hybrid approach to simulate turbulent flows by modeling the attached boundary layer with RANS, while resolving the unsteady separated flow with LES. Several studies of transonic buffet over the OAT15A airfoil have been performed by using the various versions of DES [6–8]. Deck [6] performed both standard DES and zonal DES (ZDES) of the transonic buffet over the OAT15A airfoil. In that study, ZDES predicted the self-sustained motion of the shock wave and overestimated the size of the shock-induced separation, while standard DES did not reproduce the shock motion. Grossi et al. [7] performed delayed DES (DDES) over the OAT15A airfoil and compared the results with URANS and ZDES. Huang et al. [8] performed the improved DDES (IDDES) with appropriate blending between DDES and wall-modeled LES functionality. However, the sensitivity of the prediction accuracy on the switching location between RANS and LES is a major drawback of the DES approach.

Wall-modeled LES (WMLES) is another turbulence simulation approach in which LES is deployed from the outer part of the boundary layer onward while the unresolved turbulence in the inner part of the boundary layer is modeled. The recent work of Fukushima and Kawai [9] is the first WMLES prediction of the transonic buffet over the OAT15A airfoil. In that work, a subgrid-scale model is used to compute the turbulent eddy viscosity in the LES-resolved

region, and the unresolved inner layer is modeled by solving two coupled ordinary differential equations (ODEs) for the wall-parallel velocity and the temperature. The number of total grid points in the WMLES computation is 440 million grid points, which is about two orders of magnitude higher than the above-mentioned DES simulations. The results obtained by the WMLES show good agreement with the experiments and turbulence structures are better resolved than those of ZDES, DDES, and IDDES simulations. When LES is used in all the way to the wall, the approach is called wall-resolved LES (WRLES). Because WRLES resolves the inner part of the boundary layer, higher-fidelity prediction is possible with WRLES. Garnier and Deck [10] conducted the first WRLES prediction of the transonic buffet over the OAT15A airfoil. In order to limit the required computational effort, the flow is computed in 2D RANS mode (the Spalart Allmaras model [11]) on the pressure side of the airfoil and in LES mode (The Selective Mixed Scales Model) on the suction side and in the wake. Despite the zonal treatment of the flow, 20.8 million of cells are used in their coarser grid, and twice as many are used in their finer grid. The WRLES predictions agree reasonably well with the experiments in terms of the mean field analysis and spectral analysis.

In the standard LES approach, the large-scale eddies of the flow field are resolved and the small scales are modeled using an appropriate SGS model. An alternative approach to the SGS model-based LES method is to use the numerical dissipation of the discretization scheme to account for the dissipation that takes place in the unresolved scales, leading to implicit LES (ILES). ILES benefits from its easy implementation without a SGS model and gains considerable attention from researchers in the computational fluid dynamics community [12]. This rapid growth of ILES may be attributed to the fact that research has failed to show an advantage of sophisticated SGS models over the same-cost LES with a simplistic model or even with no model and a slightly finer grid [13]. In recent years, the use of discontinuous Galerkin (DG) methods for implicit large-eddy simulation of transitional and turbulent flows has become popular in computational fluid dynamics [12, 14–20]. The numerical dissipation due to the inter-element jumps in the DG discretization acts as an implicit filter that can dissipate the unresolved turbulent features [12]. Recently, Pazner et al. [21] apply a high-order DG method to the WRLES simulation of transonic buffet on the OAT15A airfoil to study the effect of mesh refinement, polynomial degree, and artificial viscosity parameters.

In this paper, we propose an implicit matrix-free discontinuous Galerkin method for WRILES computation of transonic buffet over the OAT15A supercritical airfoil at Mach number 0.73, angle of attack 3.5° and Reynolds number 3×10^6 . In order to avoid the CFL limitation on the timestep size, we use diagonally implicit Runge-Kutta (DIRK) schemes to discretize the time derivative. We develop a Jacobian-free Newton-Krylov (JFNK) method to solve nonlinear systems arising from our spatial and temporal discretization of the Navier-Stokes equations. These methods are implemented using CUDA C/C++ with MPI-based parallelization to harness the computational power of NVIDIA GPUs. Furthermore, accurate prediction of turbulent flows at high Reynolds numbers requires a good approximation of both laminar and turbulent flows in the boundary layers. In order to adequately resolve the boundary layers, we employ a mesh refinement strategy that refines the grid toward the wall and keeps the cell aspect ratio sufficiently small.

Our WRILES method is used to predict the buffet onset, the buffet frequency, and turbulence statistics and capture various turbulence phenomena such as periodical low-frequency oscillations of shock wave in the streamwise direction, strong shear layer detached from the shock wave due to shock wave boundary layer interaction (SWBLI) and small scale structures broken down by the shear layer instability in the transition region, and shock-induced flow separation. The pressure coefficient, the root mean square (RMS) of the fluctuating pressure and the streamwise range of the shock wave oscillation are in good agreement with the experimental data [4].

The results reported in this paper demonstrate that our WRILES method can accurately predict the onset of turbulence and buffet phenomena at high Reynolds numbers without a subgrid scale model or a wall model. The successful computation of transonic buffet over the OAT15A airfoil could represent an important step toward the development and application of WRILES methods for turbulent flows at high Reynolds numbers.

The paper is organized as follows. In Section 2, we describe the numerical methodology to discretize the Navier-Stokes equations. In Section 3, we discuss and compare the obtained results with the experimental data [4], and with the available numerical experiments: ZDES [6], DDES [7], IDDES [8], and WMLES [9]. Finally, some concluding remarks and a rationale for the success of WRILES for transonic buffet prediction are presented in Section 4.

II. Methodology

A. Governing Equations

Let $t_f > 0$ be a final time and let $\Omega \subset \mathbb{R}^d$, $1 \leq d \leq 3$ be an open, connected and bounded physical domain with Lipschitz boundary $\partial\Omega$. The unsteady compressible Navier-Stokes equations in conservation form are given by

$$\mathbf{q} - \nabla \mathbf{u} = 0, \quad \text{in } \Omega \times [0, t_f], \quad (1a)$$

$$\frac{\partial \mathbf{u}}{\partial t} + \nabla \cdot \mathbf{F}(\mathbf{u}, \mathbf{q}) = 0, \quad \text{in } \Omega \times [0, t_f], \quad (1b)$$

$$\mathbf{B}(\mathbf{u}, \mathbf{q}) = 0, \quad \text{on } \partial\Omega \times [0, t_f], \quad (1c)$$

$$\mathbf{u} - \mathbf{u}_0 = 0, \quad \text{on } \Omega \times \{0\}. \quad (1d)$$

Here, $\mathbf{u} = (\rho, \rho u_j, \rho E)$, $j = 1, \dots, d$ is the m -dimensional ($m = d + 2$) vector of conserved quantities, \mathbf{u}_0 is an initial state, $\mathbf{B}(\mathbf{u}, \mathbf{q})$ is a boundary operator, and $\mathbf{F}(\mathbf{u}, \mathbf{q})$ are the inviscid and viscous fluxes of dimensions $m \times d$,

$$\mathbf{F}(\mathbf{u}, \mathbf{q}) = \begin{pmatrix} \rho u_j \\ \rho u_i u_j + \delta_{ij} p - \tau_{ij} \\ u_j (\rho E + p) - u_i \tau_{ij} + f_j \end{pmatrix}, \quad i, j = 1, \dots, d, \quad (2)$$

where p denotes the thermodynamic pressure, τ_{ij} the viscous stress tensor, f_j the heat flux, and δ_{ij} is the Kronecker delta. For a calorically perfect gas in thermodynamic equilibrium, $p = (\gamma - 1) (\rho E - \rho \|\mathbf{u}\|^2/2)$, where $\gamma = c_p/c_v > 1$ is the ratio of specific heats and in particular $\gamma \approx 1.4$ for air. c_p and c_v are the specific heats at constant pressure and volume, respectively. For a Newtonian fluid with the Fourier's law of heat conduction, the viscous stress tensor and heat flux are given by

$$\tau_{ij} = \mu \left(\frac{\partial u_i}{\partial x_j} + \frac{\partial u_j}{\partial x_i} - \frac{2}{3} \frac{\partial u_k}{\partial x_k} \delta_{ij} \right) + \beta \frac{\partial u_k}{\partial x_k} \delta_{ij}, \quad f_j = -\kappa \frac{\partial T}{\partial x_j}, \quad (3)$$

where T denotes temperature, μ the dynamic (shear) viscosity, β the bulk viscosity, $\kappa = c_p \mu / Pr$ the thermal conductivity, and Pr the Prandtl number. In particular, $Pr \approx 0.71$ for air, and additionally $\beta = 0$ under the Stokes' hypothesis.

B. Shock Capturing

To deal with shocks, we use the physics-based artificial viscosity approach introduced by Fernandez et al. [22]. This approach relies on shock, thermal gradient and shear sensors. The *shock sensor* is constructed such that

$$s_\beta(\mathbf{x}) = s_\theta \cdot s_\omega, \quad s_\theta = -\frac{h_\beta}{k} \frac{\nabla \cdot \mathbf{u}}{a^*}, \quad s_\omega = \frac{(\nabla \cdot \mathbf{u})^2}{(\nabla \cdot \mathbf{u})^2 + |\nabla \times \mathbf{u}|^2 + \varepsilon}, \quad (4)$$

where ε is a constant of the order of the machine precision squared, k is the polynomial degree and a_c is the critical speed of speed of sound. The element size is taken along the direction of the density gradient

$$h_\beta(\mathbf{x}) = h_{\text{ref}} \frac{|\nabla \rho|}{\sqrt{\nabla \rho^T \cdot \mathbf{M}_h^{-1} \nabla \rho + \varepsilon}} \quad (5)$$

where \mathbf{M}_h is the metric tensor of the mesh, and h_{ref} is the size of the reference element used in the construction of \mathbf{M}_h . In addition, we introduce the following mesh size for the artificial molecular viscosity defined later

$$h_\mu(\mathbf{x}) = h_{\text{ref}} \inf_{|\mathbf{a}|=1} \{ \mathbf{a}^T \cdot \mathbf{M}_h \mathbf{a} \}. \quad (6a)$$

The *shear sensor* is also designed to detect under-resolved features, namely velocity gradients, and is constructed from

$$s_\mu(\mathbf{x}) = \frac{h_{\text{ref}}}{k} \frac{\|\mathcal{L}(\mathbf{u}) \cdot \mathbf{x}_\xi^T\|_2}{u_{\max}} \quad (7)$$

where $\|\cdot\|_2$ denotes the Euclidean norm, u_{\max} is the maximum isentropic velocity (obtained by reversibly converting all the energy into kinetic energy)

$$u_{\max} = \sqrt{|\mathbf{u}|^2 + \frac{2}{\gamma-1} a^2}, \quad \mathcal{L}(\mathbf{u}) = \frac{\partial \mathbf{u}_i}{\partial \mathbf{x}_j} (1 - \delta_{ij}), \quad (8)$$

with δ_{ij} representing Kronecker's delta.

We then add artificial bulk viscosity and artificial molecular viscosity (β^*, μ^*) to the physical values such that:

$$\beta = \beta_f + \beta^*, \quad \mu = \mu_f + \mu^*,$$

where the amount of viscosities are determined to ensure a cell Péclet number of $\mathcal{O}(1)$ as follows

$$\beta^*(\mathbf{x}) = \hat{s}_\beta \rho \frac{k_\beta h_\beta}{k} \sqrt{|\mathbf{u}|^2 + a^{*2}} \quad (9a)$$

$$\mu^*(\mathbf{x}) = \hat{s}_\mu \rho \frac{k_\mu h_\mu}{k} \sqrt{|\mathbf{u}|^2 + a^{*2}}. \quad (9b)$$

Here $k_{\mu,\kappa} = 1$, $k_\beta = 1.5$, and $(\hat{s}_\beta, \hat{s}_\mu)$ denote the smoothly bounded values of the sensors in equations (4) and (7), and are given by

$$\hat{s}_\beta(\mathbf{x}) = \ell(s_\beta; s_{\beta,0}, s_{\beta,\max}), \quad \hat{s}_\mu(\mathbf{x}) = \ell(s_\mu; s_{\mu,0}, s_{\mu,\max}). \quad (10)$$

The function ℓ represents a smooth approximation to the following limiting function $L(s; s_0, s_{\max}) = \min\{\max\{s - s_0, 0\} - s_{\max}, 0\} + s_{\max}$. In particular, it is defined as follows

$$\ell(s; s_0, s_{\max}) = \ell_{\min}(\ell_{\max}(s - s_0) - s_{\max}) + s_{\max}, \quad (11)$$

where

$$\begin{aligned} \ell_{\max}(s) &= \frac{s}{\pi} \arctan(100s) + \frac{s}{2} - \frac{1}{\pi} \arctan(100) + \frac{1}{2}, \\ \ell_{\min}(s) &= s - \ell_{\max}(s), \end{aligned} \quad (12)$$

Here the first parameter s_0 represents the starting point of the limiting function ℓ where it begins to increase with s , while the second parameter $s_{\max} > 0$ is the upper bound of the non-negative variable s . The shock parameters are chosen as $s_{\beta,\max} = s_{\mu,\max} = 2$, $s_{\beta,0} = 0, 01$, and $s_{\mu,0} = 1$ according to Fernandez et al. [22]. Since the original artificial viscosity field (β^*, μ^*) are discontinuous, a node-averaging operator is applied to (β^*, μ^*) to make them C^0 continuous. We employ an element-wise linear reconstruction procedure introduced in [23] to smooth the metric tensor of the mesh.

C. Discontinuous Galerkin Method

Let $\Omega \subseteq \mathbb{R}^d$ with $d = 3$ be a physical domain with Lipschitz boundary $\partial\Omega$. We denote by \mathcal{T}_h a collection of disjoint, regular, k -th degree curved elements K that partition Ω , and set $\partial\mathcal{T}_h := \{\partial K : K \in \mathcal{T}_h\}$ to be the collection of the boundaries of the elements in \mathcal{T}_h . Let $\mathcal{P}^k(D)$ denote the space of complete polynomials of degree k on a domain $D \in \mathbb{R}^n$, let $L^2(D)$ be the space of square-integrable functions on D , and let ψ_K^k denote the k -th degree parametric mapping from the reference element K_{ref} to some element $K \in \mathcal{T}_h$ in the physical domain. We then introduce the following discontinuous finite element spaces:

$$\mathbf{Q}_h^k = \{\mathbf{r} \in [L^2(\mathcal{T}_h)]^{m \times d} : (\mathbf{r} \circ \psi^k)|_K \in [\mathcal{P}^k(K_{ref})]^{m \times d} \quad \forall K \in \mathcal{T}_h\},$$

$$\mathbf{V}_h^k = \{\mathbf{w} \in [L^2(\mathcal{T}_h)]^m : (\mathbf{w} \circ \psi^k)|_K \in [\mathcal{P}^k(K_{ref})]^m \quad \forall K \in \mathcal{T}_h\},$$

where m denotes the number of equations of the conservation law, i.e. $m = d + 2$ for the Navier-Stokes system. Next, we define several inner products associated with these finite element spaces as

$$(\mathbf{w}, \mathbf{v})_{\mathcal{T}_h} = \sum_{K \in \mathcal{T}_h} (\mathbf{w}, \mathbf{v})_K = \sum_{K \in \mathcal{T}_h} \int_K \mathbf{w} \cdot \mathbf{v}, \quad (13a)$$

$$(\mathbf{W}, \mathbf{V})_{\mathcal{T}_h} = \sum_{K \in \mathcal{T}_h} (\mathbf{W}, \mathbf{V})_K = \sum_{K \in \mathcal{T}_h} \int_K \mathbf{W} : \mathbf{V}, \quad (13b)$$

$$\langle \mathbf{w}, \mathbf{v} \rangle_{\partial\mathcal{T}_h} = \sum_{K \in \mathcal{T}_h} \langle \mathbf{w}, \mathbf{v} \rangle_{\partial K} = \sum_{K \in \mathcal{T}_h} \int_{\partial K} \mathbf{w} \cdot \mathbf{v}, \quad (13c)$$

for $\mathbf{w}, \mathbf{v} \in \mathbf{V}_h^k$, $\mathbf{W}, \mathbf{V} \in \mathbf{Q}_h^k$, where \cdot and $:$ denotes the scalar product and Frobenius inner product, respectively.

Note that the above spaces consist of functions that are continuous inside every element and yet discontinuous across the boundary of any two neighboring elements. In other words, the functions in these spaces are *double-valued* on the *interior* faces of the finite element mesh. Furthermore, they are *multiple-valued* at the vertices of the finite element mesh. The number of function values at any particular vertex is equal to the number of faces connected to that vertex. Therefore, DG methods often have many times more degrees of freedom than continuous finite element methods. Fortunately, the higher number of degrees of freedom comes with some important beneficial features. DG methods provide a stable high-order discretization of linear convection operators and result in diagonal-block mass matrix. The latter feature makes explicit time integration efficient for (and popular with) DG methods.

The DG discretization of the unsteady compressible Navier-Stokes equations reads as follows: Find $(\mathbf{q}_h(t), \mathbf{u}_h(t)) \in$

$\mathbf{Q}_h^k \times \mathbf{V}_h^k$ such that

$$(\mathbf{q}_h, \mathbf{r})_{\mathcal{T}_h} + (\mathbf{u}_h, \nabla \cdot \mathbf{r})_{\mathcal{T}_h} - \langle \widehat{\mathbf{u}}_h, \mathbf{r} \cdot \mathbf{n} \rangle_{\partial \mathcal{T}_h} = 0, \quad (14a)$$

$$\left(\frac{\partial \mathbf{u}_h}{\partial t}, \mathbf{w} \right)_{\mathcal{T}_h} - \left(\mathbf{F}(\mathbf{u}_h, \mathbf{q}_h), \nabla \mathbf{w} \right)_{\mathcal{T}_h} + \left(\widehat{\mathbf{f}}_h(\mathbf{u}_h, \mathbf{q}_h), \mathbf{w} \right)_{\partial \mathcal{T}_h} = 0, \quad (14b)$$

for all $(\mathbf{r}, \mathbf{w}) \in \mathbf{Q}_h^k \times \mathbf{V}_h^k$ and all $t \in [0, t_f]$, as well as

$$(\mathbf{u}_h|_{t=0} - \mathbf{u}_0, \mathbf{w})_{\mathcal{T}_h} = 0, \quad (14c)$$

for all $\mathbf{w} \in \mathbf{V}_h^k$. Here $\widehat{\mathbf{u}}_h$ is the numerical trace and $\widehat{\mathbf{f}}_h$ is the numerical flux. Different choices of the numerical trace and flux yield different DG methods. They play an important role in the stability and accuracy of the resulting DG method.

For the local DG (LDG) method [24], the numerical trace and flux are defined on the interior faces as follows

$$\begin{aligned} \widehat{\mathbf{u}}_h &= \frac{1}{2}(\mathbf{u}_h^+ + \mathbf{u}_h^-) + (\mathbf{u}_h^+ \boldsymbol{\beta} \cdot \mathbf{n}^+ + \mathbf{u}_h^- \boldsymbol{\beta} \cdot \mathbf{n}^-), \\ \widehat{\mathbf{f}}_h &= \frac{1}{2} (\mathbf{F}(\mathbf{u}_h^+, \mathbf{q}_h^+) + \mathbf{F}(\mathbf{u}_h^-, \mathbf{q}_h^-)) \cdot \mathbf{n}^+ + \boldsymbol{\sigma} \cdot (\mathbf{u}_h^+ - \mathbf{u}_h^-), \end{aligned} \quad (15)$$

where $\boldsymbol{\beta}$ is a vector-valued function and $\boldsymbol{\sigma}$ is a matrix-valued function. In this paper, we set $\boldsymbol{\beta} = 0$ and $\boldsymbol{\sigma} = \lambda_{max}(\widehat{\mathbf{u}}_h) \mathbf{I}$, where λ_{max} denotes the maximum-magnitude eigenvalue of $\mathbf{A}_n(\mathbf{u}_h) = [\partial \mathbf{F}_{\text{inv}}(\mathbf{u}_h)/\partial \mathbf{u}] \cdot \mathbf{n}$ with \mathbf{F}_{inv} being the inviscid part of the flux function \mathbf{F} . Additional details on this stabilization matrix and the resulting Riemann solver are presented in [12, 25]. Note that $\mathbf{u}_h^+ = \mathbf{u}_h|_{F \in K^+}$ and $\mathbf{u}_h^- = \mathbf{u}_h|_{F \in K^-}$ denote the restriction of the numerical solution \mathbf{u}_h on interior face F shared by elements K^+ and K^- .

On the boundary faces, the definition of the numerical trace and flux depends on the boundary conditions. For the ILES computation presented in this paper, there are two types of boundary conditions, namely, far-field condition and adiabatic wall condition. For the far-field condition, we set $\widehat{\mathbf{u}}_h = \frac{1}{2}(\mathbf{u}_h + \mathbf{u}_\infty) + \frac{1}{2}|\mathbf{A}_n(\mathbf{u}_h)|(\mathbf{u}_h - \mathbf{u}_\infty)$ and $\widehat{\mathbf{f}}_h = \mathbf{F}(\mathbf{u}_h, \mathbf{q}_h) \cdot \mathbf{n} + \boldsymbol{\sigma} \cdot (\mathbf{u}_h - \widehat{\mathbf{u}}_h)$, where \mathbf{u}_∞ denotes the freestream value of the flow variables. Note that $|\mathbf{A}_n(\mathbf{u}_h)| = \mathbf{L}|\boldsymbol{\Lambda}|\mathbf{R}$, where the matrices \mathbf{L} , $\boldsymbol{\Lambda}$, and \mathbf{R} represent the eigenvalue decomposition of the matrix $\mathbf{A}_n(\mathbf{u}_h)$. For the adiabatic wall boundary condition, we set $\widehat{\rho}_h = \rho_h$, $\widehat{\rho \mathbf{u}}_h = 0$, $\widehat{\rho E}_h = \rho E_h$, and the first and last components of the numerical flux $\widehat{\mathbf{f}}_h$ to zero.

Finally, the semi-discrete system (14) is further discretized in time using high-order, L -stable diagonally implicit Runge-Kutta (DIRK) schemes [26]. The use of high-order, L -stable methods for the temporal discretization is crucial for accuracy and robustness when dealing with turbulent shock flows at high Reynolds number.

The hybridized DG (HDG) method [12, 25] does not define the numerical trace $\widehat{\mathbf{u}}_h$ terms of the numerical solution. In the HDG method, the numerical trace becomes an additional variable to be solved by introducing another equation

that imposes the continuity of the numerical flux and enforces boundary conditions. In this paper, the LDG method is used to solve the compressible Navier-Stokes equations since it is better suited to a Jacobian-free Newton-Krylov solver than the HDG method.

D. Solution Method

The Newton's method is used to solve the nonlinear system of equations $\mathbf{R}(\mathbf{u}^n) = 0$ resulting from the temporal discretization of the system (14), where \mathbf{u}^n is the vector of degrees of freedom of \mathbf{u}_h^n and $\mathbf{R}(\cdot)$ is the residual vector. Note that the superscript n denotes the n^{th} timestep. In order to reduce the number of Newton iterations, we compute the initial guess $\mathbf{u}_h^{n,0}$ at n^{th} timestep by solving the following least-squares problem [12]:

$$\mathbf{u}^{n,0} := \sum_{j=1}^J \alpha_j \mathbf{u}^{n-j}$$

where \mathbf{u}^l denotes the solution at the l^{th} timestep, and

$$(\alpha_1, \dots, \alpha_J) = \arg \min_{(\beta_1, \dots, \beta_J) \in \mathbb{R}^J} \left\| \mathbf{R} \left(\sum_{j=1}^J \beta_j \mathbf{u}^{n-j} \right) \right\|. \quad (16)$$

This optimization problem is solved by using the Levenberg–Marquardt (LM) algorithm [27], where the gradient vectors $\partial \mathbf{R} / \partial \beta_j$ are approximated by finite differences. This initialization first proposed in [12] adds little to the overall computational cost while reducing the number of Newton iterations compared to the standard initialization using the previous solution.

In each Newton m^{th} iteration, we use GMRES to solve the resulting linear system $\mathbf{J}(\mathbf{u}^{n,m})\delta\mathbf{u}^{n,m} = -\mathbf{R}(\mathbf{u}^{n,m})$, where $\mathbf{J}(\mathbf{u}^{n,m})$ is the Jacobian matrix. To simplify the notation, we shall drop the superscript m . In order to accelerate the convergence rate of GMRES we construct a reduced basis (RB) approximation [28–30] and develop a matrix-free scalable preconditioner. Given a reduced basis matrix \mathbf{W}_n consisting of a number of previous solution vectors, the RB approximation to $\delta\mathbf{u}^n$ is computed as $\delta\mathbf{u}_{\text{rb}}^n = \mathbf{W}_n \mathbf{a}_{\text{rb}}^n$, where \mathbf{a}_{rb}^n is the solution of the RB system $\mathbf{J}_{\text{rb}}(\mathbf{u}^n)\mathbf{a}_{\text{rb}}^n = -\mathbf{R}_{\text{rb}}(\mathbf{u}^n)$ with $\mathbf{J}_{\text{rb}}(\mathbf{u}^n) = (\mathbf{W}_n \mathbf{J}(\mathbf{u}^n))^T (\mathbf{J}(\mathbf{u}^n) \mathbf{W}_n)$ and $\mathbf{R}_{\text{rb}}(\mathbf{u}^n) = (\mathbf{W}_n \mathbf{J}(\mathbf{u}^n))^T \mathbf{R}(\mathbf{u}^n)$. The RB approximation $\delta\mathbf{u}_{\text{rb}}^n$ is used as the initial solution in the GMRES method. The key idea in devising a matrix-free preconditioner lies in the construction of an approximation to the Jacobian matrix $\mathbf{J}(\mathbf{u}^n)$ through a suitable low-rank approximation. Our preconditioner has the following form:

$$\mathbf{P}_n = \mathbf{M} + \mathbf{V}_n \mathbf{D}_n^{-1} \mathbf{W}_n, \quad (17)$$

where \mathbf{M} is the mass matrix, \mathbf{V}_n and \mathbf{D}_n are chosen to satisfy the following approximation property:

$$\mathbf{P}_n \mathbf{W}_n = \mathbf{J}(\mathbf{u}^n) \mathbf{W}_n . \quad (18)$$

In order to satisfy this equation, we choose $\mathbf{D}_n = \mathbf{W}_n^T \mathbf{W}_n$ and $\mathbf{V}_n = \mathbf{J}(\mathbf{u}^n) \mathbf{W}_n - \mathbf{M} \mathbf{W}_n$. Using the Sherman–Morrison–Woodbury formula, we compute the inverse of the preconditioner \mathbf{P}_n as:

$$\mathbf{P}_n^{-1} = \mathbf{M}^{-1} - \mathbf{M}^{-1} \mathbf{V}_n \left(\mathbf{D}_n + \mathbf{W}_n^T \mathbf{M}^{-1} \mathbf{V}_n \right)^{-1} \mathbf{W}_n^T \mathbf{M}^{-1} , \quad (19)$$

The low-rank preconditioner of the form (17) can be viewed as a generalization of the BFGS update [31–34] with a distinctive feature that our approach allows for arbitrary-rank approximation, whereas the BFGS update is only a rank-two approximation of the Jacobian matrix.

The computation of $\mathbf{J}(\mathbf{u}^n) \mathbf{W}_n$ can be expensive if we have to form the Jacobian matrix $\mathbf{J}(\mathbf{u}_n)$ and perform matrix-matrix multiplication. Instead, the product of the Jacobian matrix with any vector \mathbf{y} can be approximately computed by the Taylor expansion as follows

$$\mathbf{J}(\mathbf{u}^n) \mathbf{y} \approx \frac{\mathbf{R}(\mathbf{u}^n + \epsilon \mathbf{y}) - \mathbf{R}(\mathbf{y})}{\epsilon} , \quad (20)$$

for small enough ϵ . Furthermore, since we only need to compute the first column of the matrix $\mathbf{J}(\mathbf{u}^n) \mathbf{W}_n$, it allows us to construct the preconditioner with only *one evaluation* of the residual vector. With this reduced preconditioning technique, the construction of the preconditioner adds little to the overall cost. Therefore, the computational complexity of our preconditioned GMRES is comparable to that without preconditioning.

E. Residual Calculation

As computing the residual vector is the most expensive operation in our solver, we propose to vectorize the residual calculation. The residual vector is assembled from the element residual $\mathbf{R}_e(\mathbf{u}^n)$ resulting from the volume integral $(\mathbf{F}(\mathbf{u}_h, \mathbf{q}_h), \nabla \mathbf{w})_{\mathcal{T}_h}$, the face residual $\mathbf{R}_f(\mathbf{u}^n)$ resulting from the face integral $\langle \widehat{f}_h(\mathbf{u}_h, \mathbf{q}_h), \mathbf{w} \rangle_{\partial \mathcal{T}_h}$, and the mass residual resulting from the discretization of the time derivative. For any given \mathbf{u}^n , \mathbf{q}^n is the vector of degrees of freedom of the approximate gradient $\mathbf{q}_h^n \in \mathbf{Q}_h^k$ which is obtained by solving the following equation

$$(\mathbf{q}_h^n, \mathbf{r})_{\mathcal{T}_h} = \langle \widehat{\mathbf{u}}_h^n, \mathbf{r} \cdot \mathbf{n} \rangle_{\partial \mathcal{T}_h} - (\mathbf{u}_h^n, \nabla \cdot \mathbf{r})_{\mathcal{T}_h}, \quad \forall \mathbf{r} \in \mathbf{Q}_h^k, \quad (21)$$

where $\widehat{\mathbf{u}}_h^n$ is computed from \mathbf{u}_h^n as described earlier. This step requires us to compute the inverse of the mass matrix and the right-hand side in (21). Since the inverse of the mass matrix \mathbf{M}^{-1} is already pre-computed and stored in the

construction of the preconditioner, the computation of the gradient vector \mathbf{q}^n is fast. Once \mathbf{q}^n is obtained we can compute the element residual and the face residual as described below.

For tensor product elements, the solution vector \mathbf{u}^n and the residual vector $\mathbf{R}(\mathbf{u}^n)$ are stored as three-dimensional arrays of size $(k+1)^3 \times m \times N_e$, where N_e is the number of elements. They can be viewed as matrices of $(k+1)^3$ rows and mN_e columns. Let (ξ, η, ζ) be the coordinates on the master element $[0, 1]^3$. The element residual is computed by transforming the integral on physical elements to the one on the master element and using numerical quadrature as follows

$$\mathbf{R}_e(\mathbf{u}^n) = (\mathbf{D}^\xi \otimes \mathbf{S}^\eta \otimes \mathbf{S}^\zeta) \mathbf{H}_e^\xi(\mathbf{u}^n, \mathbf{q}^n) + (\mathbf{S}^\xi \otimes \mathbf{D}^\eta \otimes \mathbf{S}^\zeta) \mathbf{H}_e^\eta(\mathbf{u}^n, \mathbf{q}^n) + (\mathbf{S}^\xi \otimes \mathbf{S}^\eta \otimes \mathbf{D}^\zeta) \mathbf{H}_e^\zeta(\mathbf{u}^n, \mathbf{q}^n). \quad (22)$$

Here $\mathbf{S}^\alpha, \mathbf{D}^\alpha, \alpha = \xi, \eta, \zeta$ are matrices of size $(k+1) \times \ell$ and related to the shape functions and their derivatives at the quadrature points on the unit interval $[0, 1]$, where ℓ is the number of quadrature points on the unit interval. Typically, we choose $\ell = k+1$. Note that $\mathbf{S}^\xi = \mathbf{S}^\eta = \mathbf{S}^\zeta$ and $\mathbf{D}^\xi = \mathbf{D}^\eta = \mathbf{D}^\zeta$ since the same polynomials are used along each direction. Furthermore, $\mathbf{H}_e^\alpha, \alpha = \xi, \eta, \zeta$ are matrices of size $(k+1)^3 \times mN_e$ and obtained from evaluating the flux function and the mapping between physical elements and the master element at the quadrature points. We use the tensor product with sum-factorization [35] to compute the element residual (22) and effectively reduce the computational complexity from $O(mN_e(k+1)^6)$ to $O(mN_e(k+1)^4)$.

Let \mathcal{F}_h^i (respectively, \mathcal{F}_h^b) be the collection of all interior (respectively, boundary) faces in \mathcal{T}_h . We have

$$\begin{aligned} \langle \widehat{\mathbf{f}}_h(\mathbf{u}_h, \mathbf{q}_h), \mathbf{w} \rangle_{\partial\mathcal{T}_h} &= \sum_{K \in \mathcal{T}_h} \langle \widehat{\mathbf{f}}_h(\mathbf{u}_h, \mathbf{q}_h), \mathbf{w} \rangle_{\partial K \setminus \partial\Omega} + \langle \widehat{\mathbf{f}}_h(\mathbf{u}_h, \mathbf{q}_h), \mathbf{w} \rangle_{\partial\Omega} \\ &= \sum_{F \in \mathcal{F}_h^i} \langle \widehat{\mathbf{f}}_h^+(\mathbf{u}_h, \mathbf{q}_h), \mathbf{w}^+ \rangle_F + \sum_{F \in \mathcal{F}_h^i} \langle \widehat{\mathbf{f}}_h^-(\mathbf{u}_h, \mathbf{q}_h), \mathbf{w}^- \rangle_F + \sum_{F \in \mathcal{F}_h^b} \langle \widehat{\mathbf{f}}_h(\mathbf{u}_h, \mathbf{q}_h), \mathbf{w} \rangle_F, \end{aligned} \quad (23)$$

where $\widehat{\mathbf{f}}_h^\pm = \widehat{\mathbf{f}}_h|_{F \in \partial K^\pm}$ and $\mathbf{w}^\pm = \mathbf{w}|_{F \in \partial K^\pm}$ for any interior face F shared by two elements K^+ and K^- . Since $\widehat{\mathbf{f}}_h^+ + \widehat{\mathbf{f}}_h^- = 0$ by the definition of the numerical flux, we obtain

$$\langle \widehat{\mathbf{f}}_h(\mathbf{u}_h, \mathbf{q}_h), \mathbf{w} \rangle_{\partial\mathcal{T}_h} = \sum_{F \in \mathcal{F}_h^i} \langle \widehat{\mathbf{f}}_h^+(\mathbf{u}_h, \mathbf{q}_h), \mathbf{w}^+ \rangle_F - \sum_{F \in \mathcal{F}_h^i} \langle \widehat{\mathbf{f}}_h^+(\mathbf{u}_h, \mathbf{q}_h), \mathbf{w}^- \rangle_F + \sum_{F \in \mathcal{F}_h^b} \langle \widehat{\mathbf{f}}_h(\mathbf{u}_h, \mathbf{q}_h), \mathbf{w} \rangle_F. \quad (24)$$

Let \mathcal{F}_h be the collection of all faces and N_f be the number of faces. We introduce the following space

$$\mathcal{M}_h^k = \{ \boldsymbol{\mu} \in [L^2(\mathcal{F}_h)]^m : (\boldsymbol{\mu} \circ \boldsymbol{\phi}^k)|_F \in [\mathcal{P}^k(F_{ref})]^m \ \forall F \in \mathcal{F}_h \},$$

where $\boldsymbol{\phi}_K^k$ denote the k -th degree parametric mapping from the reference face F_{ref} to some face $F \in \mathcal{F}_h$. As a result,

the face residual $\mathbf{R}_f(\mathbf{u}^n)$ is an array of $(k+1)^2 \times m \times N_f$ entries and computed by evaluating the following integral

$$\sum_{F \in \mathcal{F}_h^i} \left\langle \widehat{f}_h^+(\mathbf{u}_h, \mathbf{q}_h), \boldsymbol{\mu} \right\rangle_F + \sum_{F \in \mathcal{F}_h^b} \left\langle \widehat{f}_h(\mathbf{u}_h, \mathbf{q}_h), \boldsymbol{\mu} \right\rangle_F$$

for all $\boldsymbol{\mu} \in \mathcal{M}_h^k$. In particular, the face residual is computed by using the sum-factorization method as follows

$$\mathbf{R}_f(\mathbf{u}^n) = (\mathbf{S}^\xi \otimes \mathbf{S}^\eta) \mathbf{G}(\mathbf{u}^n, \mathbf{q}^n), \quad (25)$$

where $\mathbf{G}(\mathbf{u}^n, \mathbf{q}^n)$ is a matrix of size $(k+1)^2 \times mN_f$ and obtained from evaluating the numerical flux and the mapping between physical faces and the reference face at the quadrature points. Note that the face residual is computed only for faces associated with elements K^+ . It follows from (24) that when we assemble the face residual into the element residual for elements K^- we need to change the sign of the face residual.

Finally, the mass residual is the product of the mass matrix and the temporal discretization of the time derivative of the conserved variables. Therefore, it can be computed much faster than both the element residual and the face residual.

F. GPU Implementation

We note from the previous subsection that both the element residual and the face residual require a number of matrix-matrix multiplications of the form:

$$\mathbf{C} = \mathbf{A}\mathbf{B} \quad (26)$$

where \mathbf{A} is a small matrix of size $(k+1) \times (k+1)$, and \mathbf{B} is matrix of size $(k+1) \times mN$, where $N = (k+1)^2 N_e$ for the element residual and $N = (k+1)N_f$ for the face residual. As the matrix \mathbf{A} is small and constant, it is stored in GPU's shared memory to speed up the memory access. The matrix \mathbf{B} is stored in GPU's main memory. Our method of computing the residual vector as BLAS level 3 allows us to obtain maximum parallel throughput on GPUs.

Note that the face residual evaluated on an interior face must be assembled into the element residual on two elements sharing that interior face, while the face residual evaluated on a boundary face must be assembled into the element residual on an element containing that boundary face. To avoid memory-access conflicts on GPUs, the coloring scheme [36] is used to assemble the face residual into the element residual to form the residual vector. Specifically, faces that does not have the common degrees of freedom of \mathbf{u}_h are marked as the same color and the face residual on the same-coloring faces can be assembled together into the element residual at once.

The proposed discretization schemes and solution methods are written using C++ language with MPI-based parallelization and CUDA-based GPU acceleration. The CUBLAS library is used for all the BLAS operations of the code. For parallel simulations, we divide the computational domain into subdomains and each GPU is responsible for computing the part of the residual vector on its own subdomain. MPI communication across neighboring subdomains is

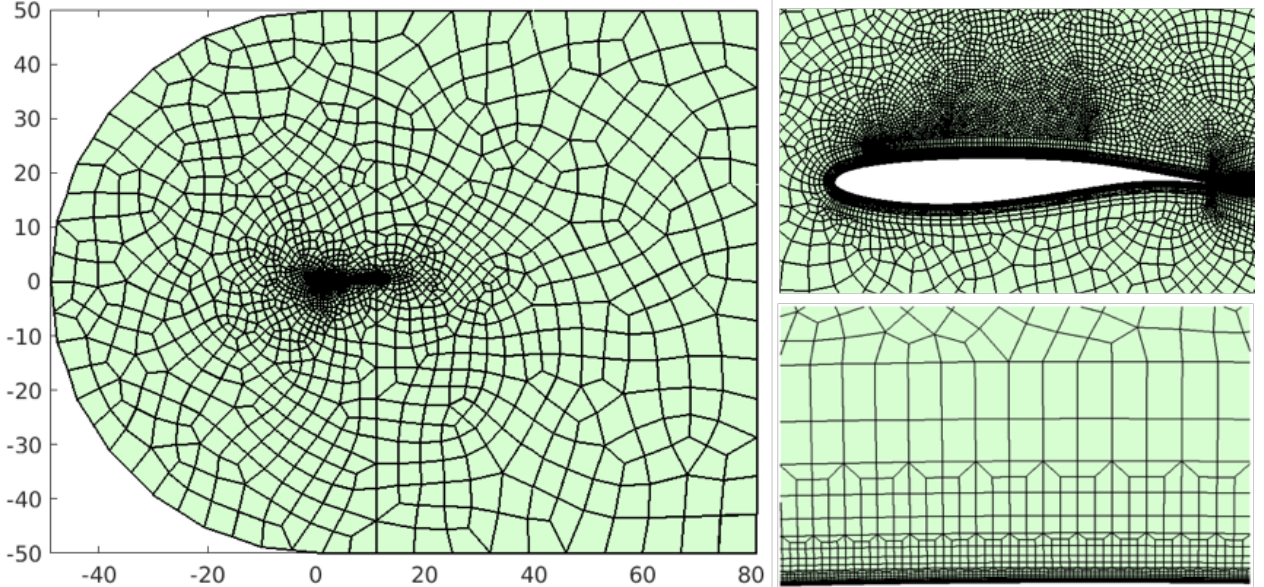


Fig. 1 Section of the mesh used for the present paper. The mesh comprises an unstructured part far from the boundary layer and a more structured part to resolve the boundary layer. The top right picture on the right shows the zoom of the mesh near the airfoil, while the bottom right picture shows the zoom of the top right picture near the wall.

overlapped with the computation of the residual vector on the interior elements of each subdomain to minimize the communication cost. All of the computations from residual calculation to iterative solvers take place inside GPUs.

III. Results and Discussions

A. Computation Description

1. Computational Mesh

The mesh used for this study is made of 1.12 million quadratic hexahedra elements, which are potentially third order accurate. For a Discontinuous Galerkin method, it represents a total of approximately 30 million nodes. The 3D mesh is obtained by extruding a 2D mesh over $0.065c$ in the z -direction, by using 32 elements, i.e 96 nodes.

As shown in Figure 1, the 2D mesh consists of both structured and unstructured grids, which are designed to resolve the boundary layers and the shock motion over the airfoil top surface. In particular, the unstructured grid is refined four times toward the wall, yielding five structured blocks. The first structured block (i.e., the most outer layer) has zero refinement. The second structured block is the first refinement, while the third (respectively, fourth, fifth) structured block is the second (respectively, third, fourth) refinement. The refinement is done by subdividing an element into two smaller elements in the streamwise direction, as shown in the bottom right part of Fig. 1. The aspect ratio of the elements is being kept less than 20 on the top surface and less than 100 on the bottom surface. The unstructured grid is generated by using the Gmsh software [37] and has two separate blocks. The first unstructured block resides on

top of the structured grid and extends from $x/c = 0.3$ to $x/c = 0.7$. It is carefully constructed to capture the shock motion of the buffet phenomenon. The second unstructured block occupies the remaining computational domain, which extends over $50c$ around the airfoil in the (x, y) plane, see Fig. 1. On the upper surface, the grid refinement is such that $\Delta x^+ \approx 15$ in the streamwise direction, $\Delta y^+ < 0.5$ in the wall normal direction, and $25 \leq \Delta z^+ \leq 45$ in the spanwise direction. On the lower surface, as the mesh is coarser, $\Delta x^+ \approx 100$, $\Delta y^+ < 1$ and $\Delta z^+ \approx 80$. Thus, the customary grid size criteria for LES of attached flows are largely satisfied on the upper surface for both the longitudinal and the wall-normal directions, but not for the spanwise direction. The spanwise criteria ($\Delta z^+ < 30$) is even less satisfied on lower surface, where the flow will probably be under-resolved.

Thanks to the very aggressive mesh refinement strategy, the 30 million nodes used by our WRILES, is comparable to the coupled RANS/LES simulations (20 million and 40 million cells for a coarse and fine mesh [10]) and lower than the 440 millions nodes of the WMLES [9].

2. Transition Trips

The mesh geometry models the transition trips as steps (see Fig. 2), with dimensions equal to the width and the granularity of the experimental trips. The trips are located at 7% of the chord length and 3 mm wide in the chord direction. On the lower surface, the trip thickness is 0.089 mm. On the upper surface, the trip thickness is 0.102 mm. These information were obtained from private communication with the authors of the experiment paper [4].

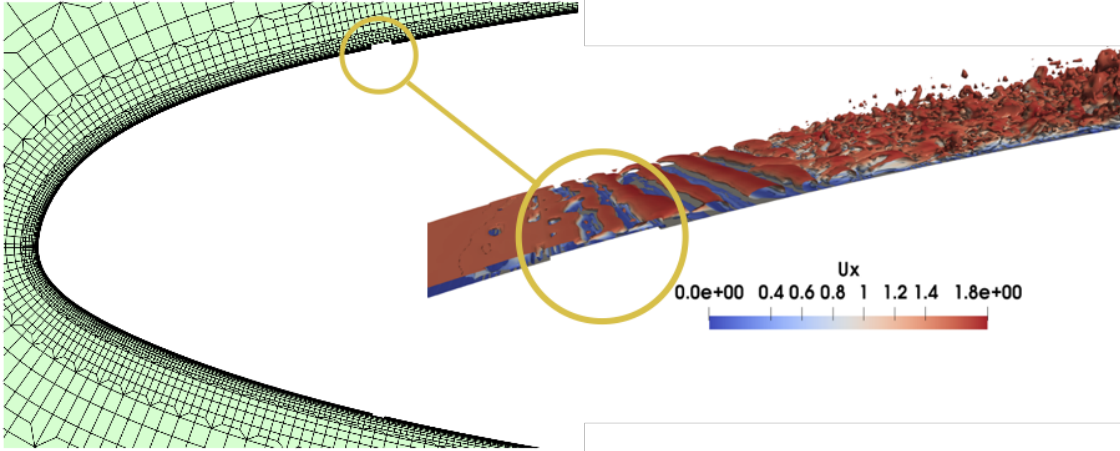


Fig. 2 Zoom of the mesh near the transition trips and the flow structure near the upper transition trip. It can be seen that the transition from laminar to turbulence occurs at the trip location. The numerical transition trips were modeled by using the dimensions of the real trips used in the experiment [4].

We emphasize the importance of the transition trips. When performing the simulation without modeling them, we do not observe the buffet phenomena. Instead we observe that the shock is stationary around $x/c = 0.6$ and that transition from laminar to turbulence occurs near the shock foot. Without the transition trips, the boundary layer on the top surface is stable all the way to the shock location because it is a supersonic boundary layer as the local Mach number

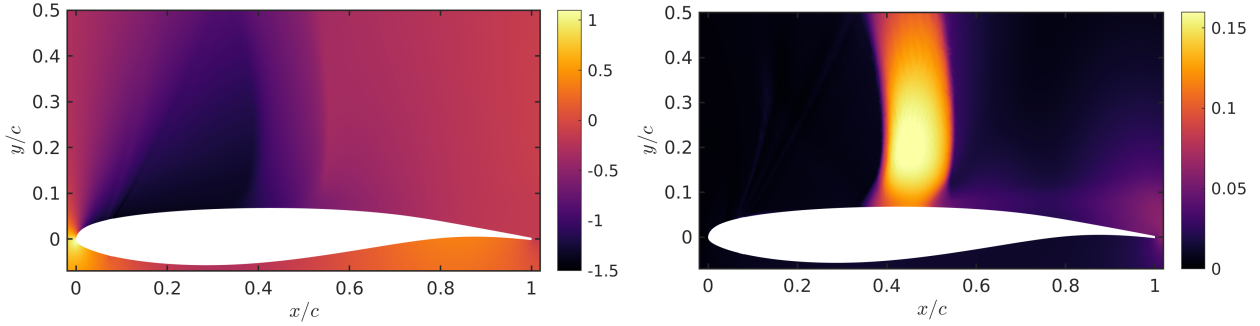


Fig. 3 Averaged pressure and its fluctuation near the airfoil for the WRILES computation: Spanwise-and-time-averaged pressure coefficient distribution (left) and pressure fluctuation distribution (right).

at the edge of the boundary layer is greater than 1. The presence of the transition trips makes the flow transition from laminar to turbulence at $x/c = 0.07$, as shown in Figure 2. The turbulent boundary layer destabilizes the shock and triggers the shock motion, leading to the buffet phenomena. Therefore, the transition trips have a very significant impact on the onset of turbulence and buffet phenomena.

Note that previous work [6–9] did not consider transition trips to trigger transition. Instead transition was prescribed by using trip terms of the turbulence model [6–8] or modifying the eddy viscosity at the transition location [9].

3. Computational Time

The numerical study is performed with a non-dimensional time step $\Delta t = 10^{-4}c/u_\infty$, and for a total of 95 chord-based time units tu_∞/c . Starting from an extruded 2D solution, the shock oscillations start after $tu_\infty/c \approx 20$. Discarding the initial transient flow, we can record up to 5 full periodic oscillations of the shock, which are used to perform the statistical data presented below. Note that one periodic shock oscillation is defined as the time period in which the shock wave moves from the most upstream position to the downstream and reaches the most upstream position again. One periodic shock oscillation takes slightly less than 14 chord-based time units. The whole computation was performed using 32 NVIDIA V100 GPUs at the Barcelona Supercomputer Center for approximately 700 run-time hours.

B. Flow Statistics and Comparisons to Experiment

1. Mean and Variance of Pressure Fields

The pressure coefficients C_p displayed on Fig. 3 and 4 are spanwise-averaged and time-averaged over 5 buffet oscillations cycles. The pressure standard deviations P_{rms} are also spanwise-averaged. Comparisons with experimental data [4], as well as numerical other numerical simulations (ZDES [6], DDES [7], IDDES [8], and WMLES [9]) are shown in Fig. 4. The pressure coefficient and fluctuations obtained by the WRILES agree very well with the experimental data. The pressure coefficient on the suction side decreases rapidly over a short distance from the leading edge to the transition location $x/c = 0.07$ and flattens out from the transition location to $x/c = 0.35$. There is no sharp variation of

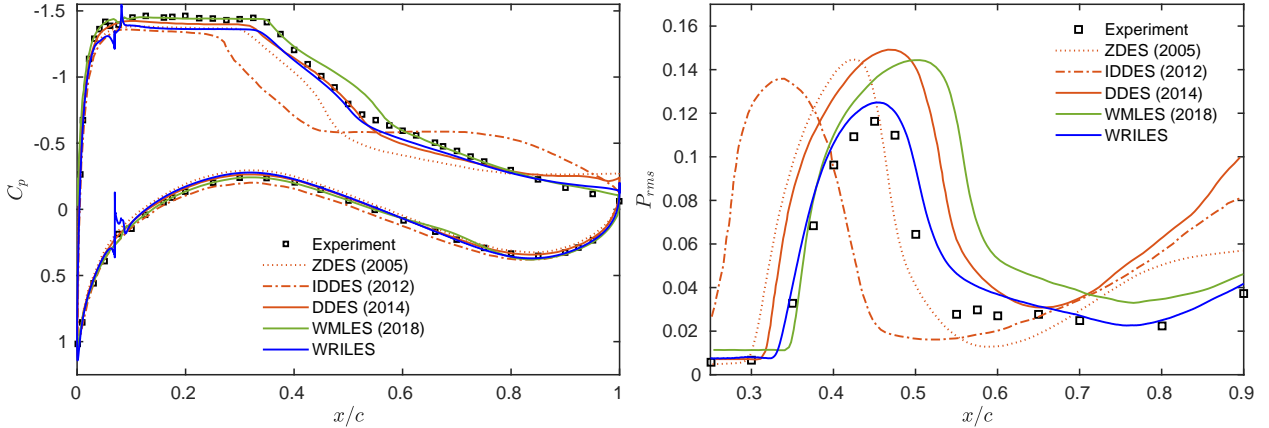


Fig. 4 Comparisons of the spanwise-and-time-averaged pressure coefficient on the airfoil surface (left) and wall pressure fluctuations on the suction surface (right). The WRILES predictions agree well with the experimental data [4]. The overshoots of the pressure coefficient around $x/c = 0.07$ obtained by the WRILES are due to the transition trips.

the pressure coefficient that would be typical of a steady shock (see Fig. 3). Instead, the averaged pressure smoothly increases over $x/c \in [0.35, 0.55]$ due to the shock motion in this range. Finally, it slowly increases over a longer distance from $x/c = 0.55$ to the trailing edge. The average location of the shock is very precisely captured, and the averaged pressure in the turbulent boundary layer is slightly overestimated upstream of the shock wave (see Fig. 4). Behind the shock wave ($x/c \geq 0.6$), the agreement is also fairly good, suggesting that the turbulent reattachment behind the shock wave is correctly predicted by the WRILES computation. Note that the pressure coefficient obtained by the WRILES has small overshoots around $x/c = 0.07$, while those obtained by other computations are smooth there. The overshoot is due to the transition trips in the WRILES computation, whereas other computations do not employ such trips. The computed pressure fluctuations are high in the shock motion range $x/c \in [0.35, 0.55]$, with a maximum value of 0.12 at $x/c = 0.46$ (see the right parts of Fig. 3 and 4). The fluctuations tend to level off downstream of the shock area, for $x/c \in [0.6, 0.8]$, and then increase again while approaching the trailing edge, for $x/c > 0.8$.

When compared to other published numerical experiments (Fig. 4), the WRILES arguably predicts the best pressure distribution on the whole upper side of the wing. Both the DDES and the WMLES can also predict a fairly accurate distribution of C_p . However, they tend to predict the region of the shock-wave oscillation slightly downstream. The same observation applies to the coupled RANS/LES results [10], which are not reported here. The WRILES can locate that region more accurately, as illustrated by the peak of pressure fluctuations in the region of $x/c \in [0.35, 0.55]$, see Fig. 4. Moreover, the amplitude of the fluctuations agrees well with the experiment, and shows that the strength of the shock wave is also better predicted by the WRILES approach. Thus, the pressure field statistics in the range $[0.35, 0.55]$, which are typical of transonic buffet, are all accurately modeled by the WRILES. Finally, the accurate prediction of the pressure fluctuations in the region of the attached turbulent boundary layer upstream of the shock seems to indicate that the fluctuations of the inner-layer turbulence are resolved well enough with WRILES.

2. Mean and Variance of Velocity Fields

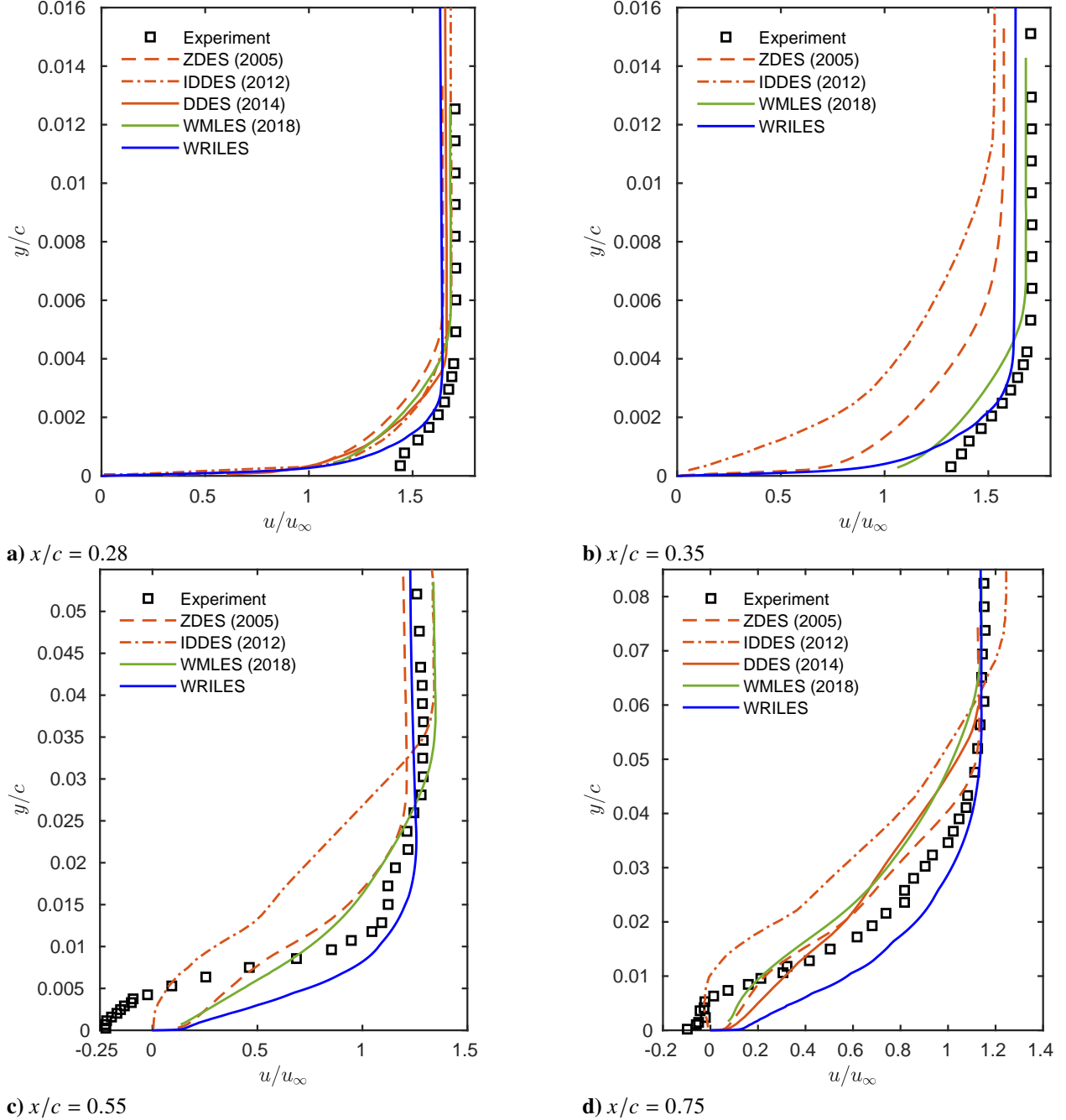


Fig. 5 Spanwise-and-time-averaged streamwise velocity profiles on the suction surface compared with experimental data and others numerical experiments. Note that y is the distance from the wall in the vertical direction.

Figure 5 displays spanwise-and-time-averaged streamwise velocity profiles at $x/c = 0.28, 0.35, 0.55$, and 0.75 for several DES and LES computations in comparison with the experimental data. At the upstream of the shock wave $x/c = 0.28$ in the fully developed attached TBL region, the WRILES predicts well the experimental mean bulk

velocity in the upper part of the boundary layer $y/c \in [0.001; 0.004]$, whereas the ZDES, DDES, IDDES and WMLES underpredict the bulk velocity. The WRILES slightly underpredicts the experimental data in the region of $y/c > 0.004$, and in the lowest part of the TBL ($y/c < 0.001$), the velocity profile given by the WRILES follows a log law, contrary to the experiments. The same observations apply for $x/c = 0.35$, where the DES-based computations predict streamwise velocities even farther from the experiments. Behind the shock wave at $x/c = 0.55$, the WRILES predicts the bulk velocity well for $y/c > 0.02$, while the WMLES shows slightly higher mean bulk velocity than the experiments. Interestingly, none of the computations capture the average flow reversal for $y/c < 0.01$. Although the WRILES predicts a reverse flow at some stage of the buffet cycle (see Fig. 9), that reversal is not strong or long enough to reverse the averaged velocity profile. At the downstream location $x/c = 0.75$, the results obtained by the WRILES and all the other computations show relatively good agreement with the experiments.

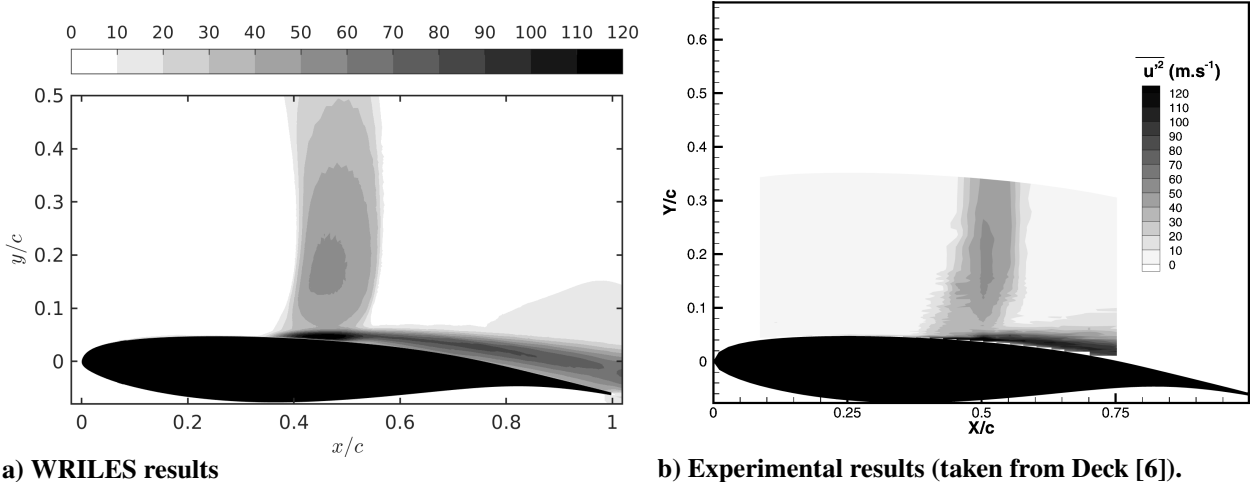


Fig. 6 Streamwise velocity fluctuations $\sqrt{u_1^{*'} u_1^{*''}}$ obtained by WRILES, and corresponding experimental results.

Fig. 6 shows the dimensionalized streamwise velocity fluctuations $u_{\text{rms}} = \sqrt{u_1^{*'} u_1^{*''}}$ over 5 shock buffet cycles and the experimental result [4]. We observe that the WRILES prediction matches well with the experimental result. The distribution of the streamwise velocity fluctuations is quite similar to that of the pressure fluctuations. However, the velocity fluctuations are larger in the separation region near the wall, while the pressure fluctuations are larger in the buffet region above the wall. These results are also qualitatively similar to those of the WMLES [9]) and the ZDES [6].

Figure 7 shows the standard deviations of the non-dimensional streamwise velocity profiles u_{rms}/u_∞ on the suction surface. In the region of the fully developed attached TBL, at $x/c = 0.28$, only the WMLES results reproduce the experiments with some accuracy, while the WRILES underestimates the velocity fluctuations and the DES-based computations predict almost no fluctuation close to the wall. At $x/c = 0.35$, both the WMLES and WRILES predict the fluctuations very well, while they are severely overestimated by the ZDES and IDDES computations. At $x/c = 0.55$, the WRILES gives good predictions near the wall $y/c \leq 0.07$ and in the log layer $y/x \geq 0.35$. In contrast, the IDDES

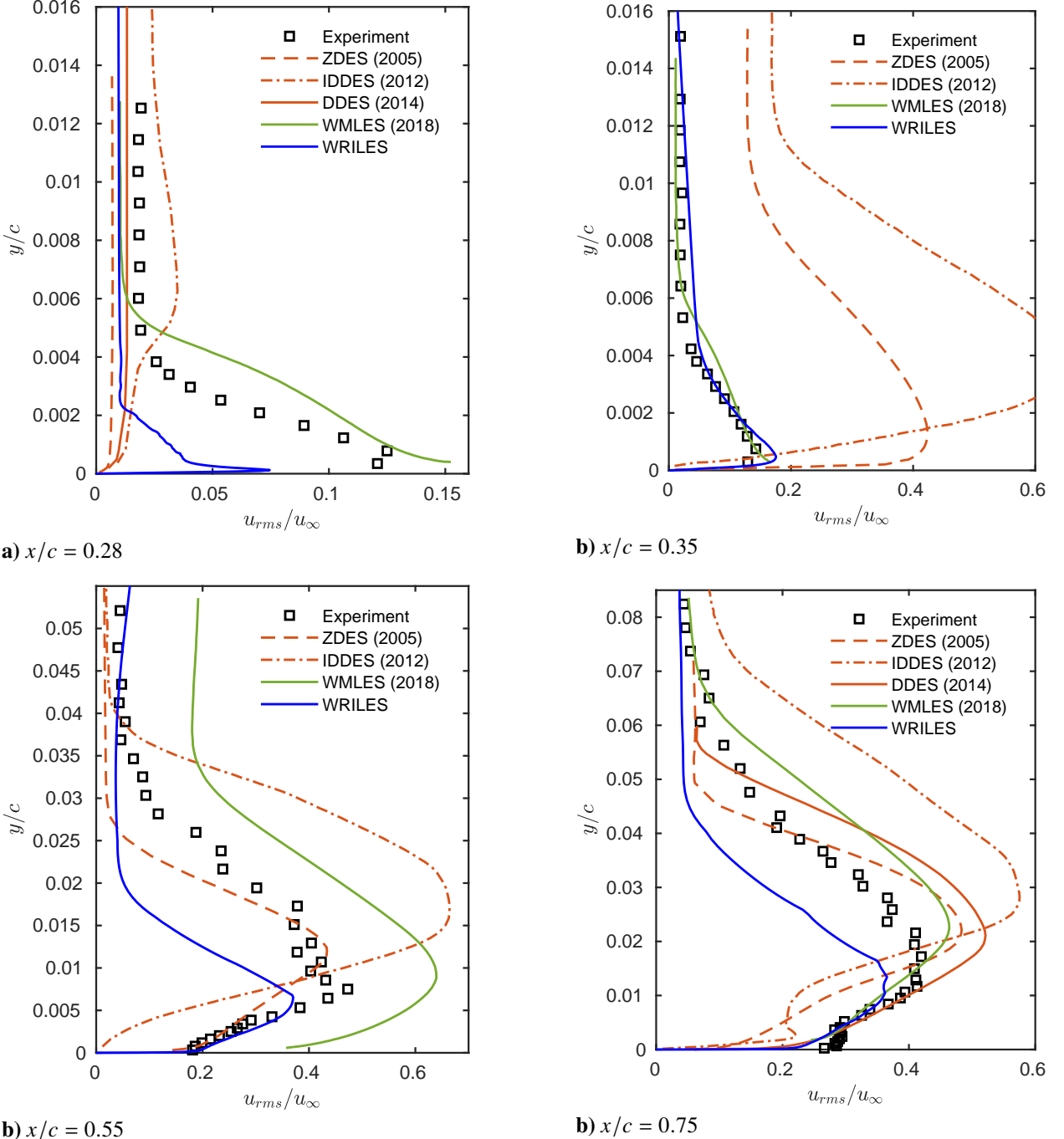


Fig. 7 Standard deviations of the streamwise velocity profiles on the suction surface compared with experimental data and other numerical experiments. Note that y is the distance from the wall in the vertical direction.

and WMLES both overestimate the velocity fluctuations inside and above the shear layer. For the WMLES, this observation may be explained by the prediction of the shock location slightly downstream of the experiments. Behind the shock-wave/boundary-layer interactions at $x/c = 0.75$, all the computations quantitatively predict the experiments reasonably well. Overall, we observe some significant differences in the standard deviations of the velocity profiles

among the simulation results.

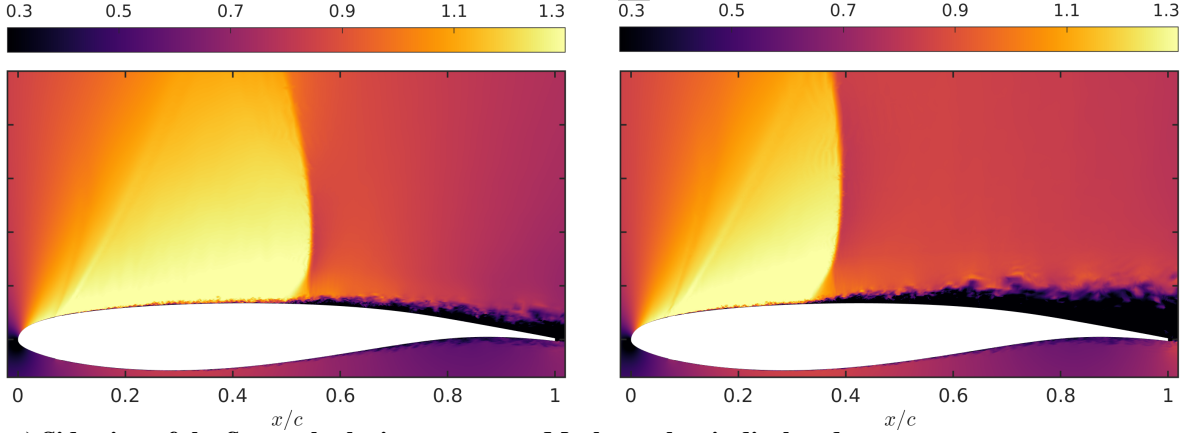
We do not report the velocity profiles from the coupled RANS/LES computations [10] on Fig. 5 and 7. Although the authors compared their results with different experimental data (these were averaged on a much shorter time), they were able to show excellent agreements for the profiles at $x/c = 0.28$ and 0.75 . However, since the RANS/LES computations did not locate accurately the shock motion range, the predicted velocity profiles at $x/c = 0.35$ and 0.55 remained significantly different from the experiment.

Overall, we see that the WRILES results match the experimental data better than the DES-based results, probably owing to the fact that the WRILES method resolves the turbulent boundary layer more accurately than other methods. While all the computations perform similarly at $x/c = 0.75$, the WRILES arguably predicts the most accurate velocity profiles near the shock region ($x/c = 0.35$ and 0.55), which is likely related to the accurate prediction of the range of the shock motion. However, very close to the wall in the attached turbulent boundary layer, the predictions of both velocity and pressure are less accurate than the WMLES and RANS/LES computations. As the velocity fluctuations are significantly underpredicted there, some features of the attached TBL must still be under-resolved with the mesh currently used. Since our mesh uses only 96 points in the spanwise direction, compared to 280 points for the RANS/LES [10] and 565 for the WMLES [9], the under-resolution in the spanwise direction is likely to be blamed. Nonetheless, Garnier and Deck [10] observed that the accurate resolution of the attached TBL does not imply the right prediction of the shock motion range. We observe that the opposite is also true : the under-resolution of the upstream TBL does not prevent the WRILES computation to make accurate predictions in the shock region and downstream.

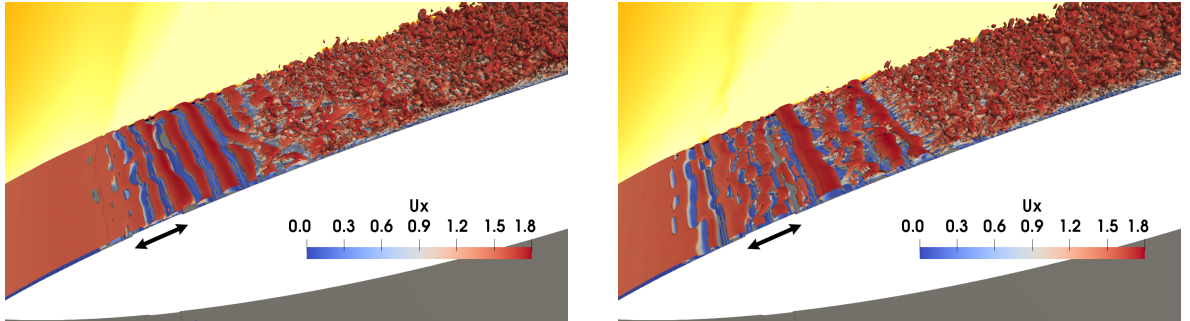
C. Dynamics of the Transonic Buffet

1. Instantaneous Flow Structures

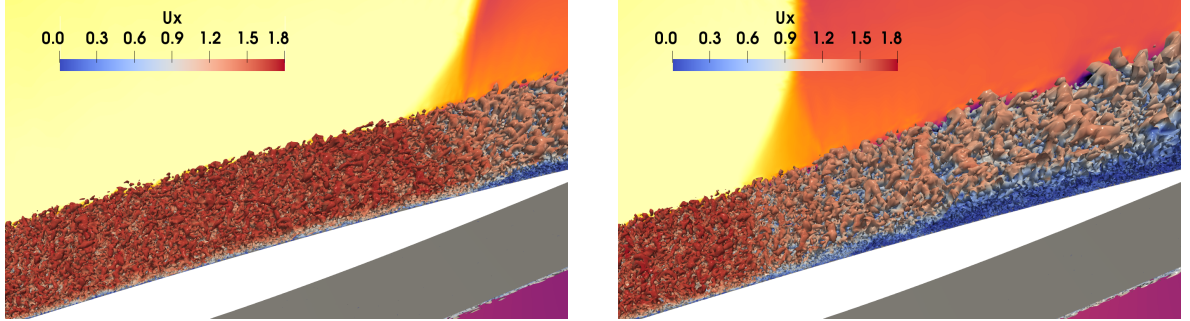
In order to visualize the instantaneous vortex structures of the flow, Fig. 8 displays the isosurfaces of Q , the second invariant of the velocity gradient tensor given by $Q = \frac{1}{2}(\text{tr}(\nabla\mathbf{u})^2 - \text{tr}(\nabla\mathbf{u}^2))$. On Fig. 8, the isosurfaces are colored by the streamwise velocity, and a spanwise cross section of the Mach number field is also displayed in the background. At $x/c = 0.07$, the transition trip generates an expansion wave, visible on the Mach number plots (Fig. 8,a-b). Two-dimensional spanwise-coherent vortices are induced by the trip and immediately break down to smaller three-dimensional structures (Fig. 8,b). Quasi-streamwise vortices and irregular lambda-shape vortices are visible in the lower part of the boundary layer, where the two-dimensional vortices breaks down at $x/c \approx 0.10$. The transition happens very fast and the boundary layer seems fully turbulent for $x/c > 0.12$. Packets of hairpin-like vortices are visible in the shock foot area, and they grow toward the downstream (Fig. 8,c). As expected, the turbulent boundary layer significantly thickens after passing through the foot shock. From Fig. 8,d), it is clear that during the upstream excursion of the shock, the shear layer is thicker and completely separated downstream of the lambda shock, while during the downstream shock excursion, the shear layer is thinner and remains largely attached to the wall, except very locally at the trailing edge.



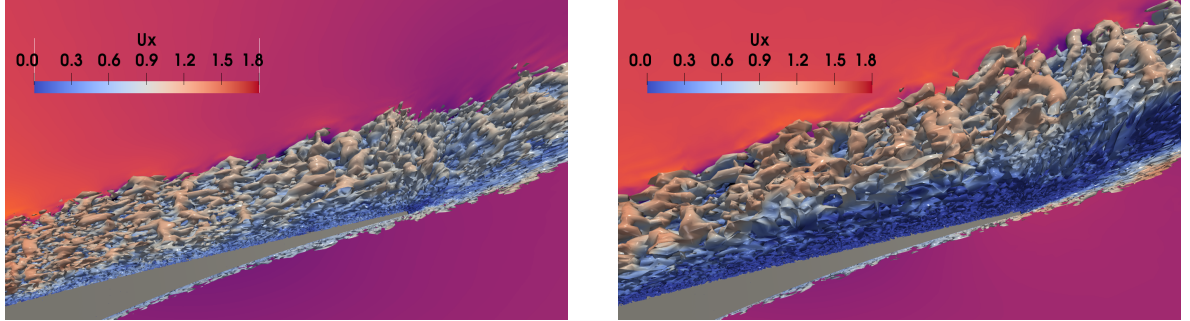
a) Side view of the flow, only the instantaneous Mach number is displayed



b) Flow structure near the transition trip



c) Flow structure near the shock foot



d) Flow structure near the trailing edge

Fig. 8 Instantaneous Mach number at $z = 0$ and isosurfaces of Q-criterion ($Q/M_\infty^2 = 200$) colored by the streamwise velocity obtained by WRILES. Left column : maximal downstream shock location ($t u_\infty/c = t_0$). Right column: maximal upstream shock location ($t = t_0 + 0.5T_s$). On b), the trip width is indicated with an arrow.

All these observations are consistent with the experiment [4], with the Q-criteria analysis of the WMLES [9] computation, and with the coupled RANS/LES [10] results. Therefore, the WRILES seems to resolve most of the medium-to-small-scales vortices that are found over the airfoil during the shock buffet cycle, although the smallest scales are probably under-resolved (see subsection III.B.2). In contrast, ZDES [6], IDDES [8], and DDES [7] computations seem unable to resolve the small vortex structures, and their predicted flow remains essentially two-dimensional even far downstream from the lambda shock.

2. Dynamics of the Shock Wave Boundary Layer Interaction

Figure 9 shows instantaneous streamwise velocity u_1 and instantaneous magnitude of the density gradient $||\nabla\rho||$ at different stages of the buffet cycle for the WRILES simulation. In the streamwise velocity snapshots (Fig. 9a-9f), the white areas indicate the separated flow regions where $u_1 < 0$.

The lambda structure of the shock foot is clearly observable in the density gradient snapshots (Fig. 9g-9l), and the vortices in the turbulent boundary layer noticeably grow as they pass through the shock foot. During the downstream excursion of the shock (first four rows of Fig. 9), as the effective shock Mach number is reduced, the shock is weaker and the flow remains largely attached. The turbulent shear layer stays near the wall, as shown on the velocity snapshots (Fig. 9a-9d). Moreover, the rear shock of the lambda structure has a larger density gradient than the upstream oblique compression wave. During the upstream shock excursion (last three rows of Fig. 9), the effective Mach number is higher and the shock stronger, inducing a large separation of the turbulent shear layer (Fig. 9d-9f). The lambda shock foot widens, the rear shock becomes weaker while the oblique shock strengthens (Fig. 9j-9l). Furthermore, the shock travels upstream faster than it travels downstream, which was also predicted by [9].

All these predictions are qualitatively similar to the experimental Schlieren pictures [4], to the WMLES results [9], and are typical of a shock buffet cycle [3]. Contrary to the WMLES, the WRILES does not predict any compression wave train downstream of the shock foot. However, Jacquin et al. [4] suggested that the wave trains observed during the experiment may be due to three-dimensional effects at the side walls of the wind tunnel, which are not modeled in the present study.

3. Power Spectral Analysis and Pressure Waves

Several theories have been proposed to explain the mechanisms governing the transonic shock buffet (see the review by Giannelis et al. [3]). Some popular explanations involve an aeroacoustic feedback loop between the shock and the trailing edge pressure perturbations. Lee [38] suggested that the fluctuations of the shock foot generate hydrodynamic instability waves propagating downstream in the turbulent shear layer. When these perturbations reach the sharp trailing edge, they generate acoustic waves traveling upstream above the shear layer. Finally, the upstream pressure waves exchange energy with the shock wave, which completes the feedback loop. Jacquin et al. [4] enriched the previous

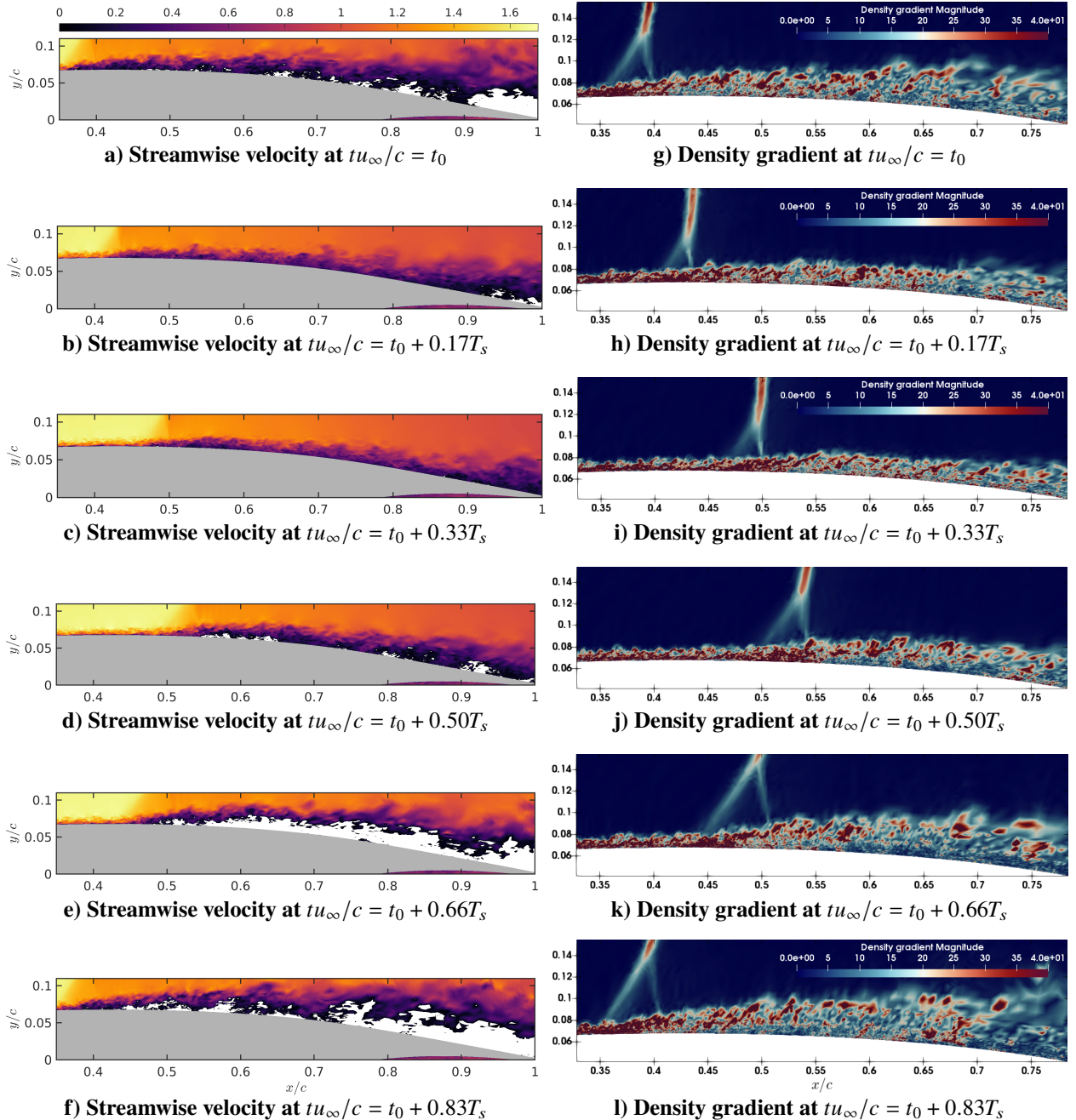
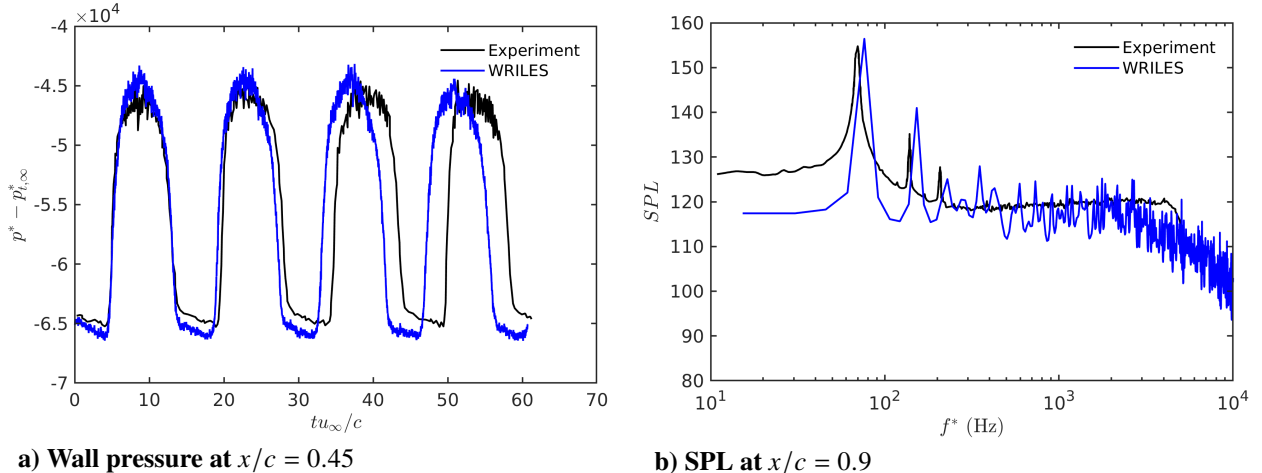


Fig. 9 Left column: instantaneous streamwise velocity u_1 at different stages of the buffet cycle. White areas indicates $u_1 < 0$. Right column: instantaneous magnitude of the density gradient $\|\nabla \rho\|$ at the same stages.

feedback mechanism considering also acoustic waves propagating along the lower surface of the wing, turning around the leading edge and hitting the shock from upstream. Hartmann et al. [39] proposed another acoustic feedback loop, where the shock motion drives the strength of the vortices generated at the shock foot. As these vortices impinge on the trailing edge, they generate acoustic waves with varying sound pressure levels which propagate upstream before interacting with the shock. In this feedback loop, the shock motion is driven by the sound pressure levels at the trailing



a) Wall pressure at $x/c = 0.45$

b) SPL at $x/c = 0.9$

Fig. 10 Time history of dimensionalized wall pressure in the shock region (left), and power spectral density of wall pressure fluctuation near the trailing edge (right).

edge. The influence of the the acoustic waves on the shock dynamics was experimentally investigated by Alshabu & Olivier [40], supporting the findings of Hartmann et al. [39].

Therefore, it seems that a numerical simulation has to solve accurately the pressure wave-field in order to deliver accurate shock buffet predictions. The present subsection assesses the WRILES ability to model all the pressure perturbations involved in the buffet feedback mechanism.

Figure 10-a) displays the time history of the wall pressure computed by the WRILES at $x/c = 0.45$, compared with the experiment. The low frequency large amplitude oscillations are due to the periodic shock motion. While the amplitude is correct, the buffet frequency is overpredicted. As observed in the experiment, when the shock location is downstream of the pressure sensor, there is little pressure fluctuation, and when the shock is upstream of the sensor, the pressure fluctuations are stronger. It indicates that the WRILES predicts the abovementioned pressure perturbations generated at the shock foot and propagating downstream in the TBL.

An autoregressive power spectral density (PSD) estimate of the wall pressure has been computed, via the Burg's method, as advised by Deck [6]. Figure 10-b) shows the PSD of the wall pressure fluctuations at $x/c = 0.9$ expressed in terms of sound pressure level (SPL), in decibels. The main peak corresponds to the main frequency of the shock periodic motion. The WRILES slightly overpredicts the buffet frequency (76 Hz instead of 69 Hz for the experiment). However such overprediction is quite common, and was also observed with ZDES [10], IDDES [8], DDES [7], and to a lesser extend with the coupled RANS/LES [10]. On the other hand, both ZDES [6] and WMLES [9] could predict the correct buffet frequency. The WRILES correctly captures the three first harmonics, but also predicts a fourth one, which is not present in the experiment, suggesting that the WRILES may overestimate the periodicity of the flow. Below 100 Hz, the lower-frequency spectrum is underpredicted, probably because the pressure signal is not long enough to compute an accurate PSD estimate in this frequency band. In the high-frequency region, the predicted PSD agrees

reasonably well with the experiment. The rather flat PSD at high frequency (400 to 4000 Hz), is reproduced by the computation, and the WRILES correctly predicts the drop of SPL for the highest frequencies (>4000 Hz). As the flat high frequency spectrum is due to the various scales of the turbulent structures, these results suggest that a large range of turbulence scales are resolved by the WRILES.

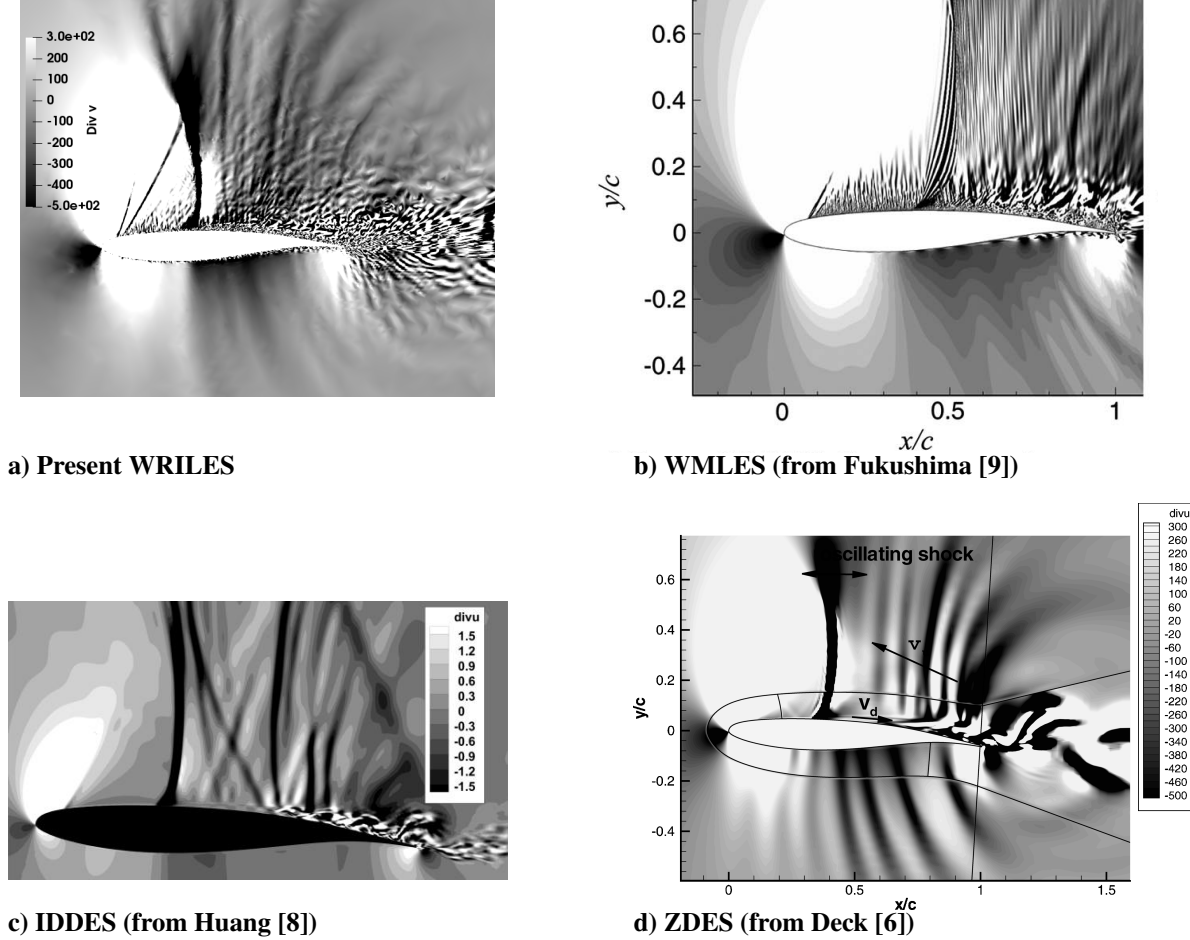


Fig. 11 Instantaneous dilatation fields $\nabla \cdot \mathbf{u}$.

In order to visualize the complete pressure wave-field, the instantaneous divergence fields of velocity $\nabla \cdot \mathbf{u}$ obtained by the present WRILES, WMLES, IDDES and ZDES are displayed in Figure 11. All simulations predict the low frequency upstream propagating acoustic waves generated when the shear layer instabilities impinge on the trailing edge. Both WRILES and ZDES predicts acoustic waves propagating along the lower surface. However, with WRILES we can not see these waves rounding the leading edge and interacting with the shock from upstream, as speculated by Jacquin et al. [4]. Both the WRILES and WMLES also show small-scale structures and high frequency acoustic waves, some of which may be numerical artifacts like the vertical wave train predicted by WMLES or the noisy wake predicted by WRILES. Indeed, our mesh is aggressively coarsened in the immediate wake area, where the elements are

very stretched. When the small turbulent structures enter this area, they become severely under-resolved (see Fig. 8-d), generate high frequency oscillations and possibly spurious pressure waves before being tamed by the artificial viscosity and the natural DG dissipation. Fig. 11-a shows that WRILES predicts upstream pressure waves originating from both the trailing edge and from the uncommonly noisy wake. Thus, we speculate these last spurious pressure waves may cause the overestimation of the buffet frequency by the present WRILES.

IV. Conclusions

In this paper, we perform a wall-resolved implicit large eddy simulation of transonic buffet phenomena over the OAT15A supercritical airfoil using the implicit discontinuous Galerkin solver. We develop a Jacobian-free Newton-GMRES method to solve the nonlinear systems arising from the DG discretization. This allows the DG solver to scale well on GPUs. In order to effectively resolve the boundary layers at high Reynolds numbers, we use a mesh refinement strategy to provide adequate resolution in the boundary layer region to capture flow transition and onset of turbulence. Without making use of either subgrid scale models or wall models, the WRILES method successfully predicts the buffet onset, the buffet frequency, and turbulence statistics. Various turbulence phenomena are predicted and demonstrated, such as periodic low-frequency oscillations of shock wave in the streamwise direction, strong shear layer-detached from the shock wave due to shock wave boundary layer interaction (SWBLI) and small scale structures broken down by the shear layer instability in the transition region, and shock-induced flow separation. The pressure coefficient, the root mean square (RMS) of the fluctuating pressure and the streamwise range of the shock wave oscillation agree well with experimental data.

Acknowledgments

The authors gratefully acknowledge NASA (under grant number NNX16AP15A) and the AFOSR (under grant number FA9550-16-1-0214) for supporting this work. Also, the authors thank the Barcelona Supercomputing Center which has provided access to its GPU cluster.

References

- [1] Hilton, W., and Fowler, R., *Photographs of shock wave movement*, National Physical Laboratories, 1947.
- [2] Lee, B., “Self-sustained shock oscillations on airfoils at transonic speeds,” *Progress in Aerospace Sciences*, Vol. 37, No. 2, 2001, pp. 147–196.
- [3] Giannelis, N. F., Vio, G. A., and Levinski, O., “A review of recent developments in the understanding of transonic shock buffet,” *Progress in Aerospace Sciences*, Vol. 92, 2017, pp. 39–84. doi:<https://doi.org/10.1016/j.paerosci.2017.05.004>.
- [4] Jacquin, L., Molton, P., Deck, S., Maury, B., and Soulevant, D., “Experimental study of shock oscillation over a transonic

supercritical profile,” *AIAA Journal*, Vol. 47, No. 9, 2009, pp. 1985–1994. doi:10.2514/1.30190, URL <http://arc.aiaa.org/doi/10.2514/1.30190>.

- [5] Thiery, M., and Coustols, E., “Numerical prediction of shock induced oscillations over a 2D airfoil: Influence of turbulence modelling and test section walls,” *International Journal of Heat and Fluid Flow*, Vol. 27, No. 4, 2006, pp. 661–670. doi:10.1016/j.ijheatfluidflow.2006.02.013.
- [6] Deck, S., “Numerical simulation of transonic buffet over a supercritical Airfoil,” *AIAA Journal*, Vol. 43, No. 7, 2005, pp. 1556–1566. doi:10.2514/1.9885, URL <http://arc.aiaa.org/doi/10.2514/1.9885>.
- [7] Grossi, F., Braza, M., and Hoarau, Y., “Prediction of transonic buffet by delayed detached-eddy simulation,” *AIAA Journal*, Vol. 52, No. 10, 2014, pp. 2300–2312. doi:10.2514/1.J052873, URL <http://arc.aiaa.org/doi/10.2514/1.J052873>.
- [8] Huang, J., Xiao, Z., Liu, J., and Fu, S., “Numerical investigation of shock buffet on an OAT15A airfoil and control effects of vortex generators,” *50th AIAA Aerospace Sciences Meeting*, 2012, pp. AIAA-2012-0044. doi:doi:10.2514/6.2012-44, URL <https://doi.org/10.2514/6.2012-44>.
- [9] Fukushima, Y., and Kawai, S., “Wall-modeled large-eddy simulation of transonic airfoil buffet at high Reynolds number,” *AIAA Journal*, Vol. 56, No. 6, 2018, pp. 2372–2388. doi:10.2514/1.J056537, URL <https://arc.aiaa.org/doi/10.2514/1.J056537>.
- [10] Garnier, E., and Deck, S., “Large-eddy simulation of transonic buffet over a supercritical airfoil,” Springer Berlin Heidelberg, Berlin, Heidelberg, 2010, pp. 135–141.
- [11] Spalart, P. R., and Allmaras, S. R., “A one-equation turbulence model for aerodynamic flows,” *La Recherche Aerospatiale*, Vol. 1, 1994, pp. 5–21. doi:10.2514/6.1992-439, URL <http://www.mendeley.com/research/a-oneequation-turbulence-model-for-aerodynamic-flows/>.
- [12] Fernandez, P., Nguyen, N. C., and Peraire, J., “The hybridized discontinuous Galerkin method for implicit large-eddy simulation of transitional turbulent flows,” *Journal of Computational Physics*, Vol. 336, 2017, pp. 308–329. doi:10.1016/j.jcp.2017.02.015.
- [13] Spalart, P. R., “Strategies for turbulence modelling and simulations,” *International Journal of Heat and Fluid Flow*, Vol. 21, Elsevier, 2000, pp. 252–263. doi:10.1016/S0142-727X(00)00007-2, URL <https://www.sciencedirect.com/science/article/pii/S0142727X00000072>.
- [14] Beck, A. D., Boellmann, T., Flad, D., Frank, H., Gassner, G. J., Hindenlang, F., and Munz, C.-D., “High-order discontinuous Galerkin spectral element methods for transitional and turbulent flow simulations,” *International Journal for Numerical Methods in Fluids*, Vol. 76, No. 8, 2014, pp. 522–548. doi:10.1002/fld.3943, URL <http://doi.wiley.com/10.1002/fld.3943>.
- [15] Frere, A., Hillewaert, K., Chivae, H. S., Mikkelsen, R. F., and Chatelain, P., “Cross-validation of numerical and experimental studies of transitional airfoil performance,” *33rd Wind Energy Symposium*, AIAA SciTech Forum, American Institute of Aeronautics and Astronautics, 2015. doi:doi:10.2514/6.2015-0499, URL <https://doi.org/10.2514/6.2015-0499>.

- [16] Gassner, G. J., and Beck, A. D., “On the accuracy of high-order discretizations for underresolved turbulence simulations,” *Theoretical and Computational Fluid Dynamics*, Vol. 27, 2013, pp. 221–237. doi:10.1007/s00162-011-0253-7.
- [17] Murman, S. M., Diosady, L., Garai, A., and Ceze, M., “A space-time discontinuous-Galerkin approach for separated flows,” *54th AIAA Aerospace Sciences Meeting*, 2016, pp. AIAA–2016–1059. doi:doi:10.2514/6.2016-1059, URL <https://doi.org/10.2514/6.2016-1059>.
- [18] Renac, F., de la Llave Plata, M., Martin, E., Chapelier, J. B., and Couaillier, V., “Aghora: A high-order DG solver for turbulent flow simulations,” Springer International Publishing, Cham, 2015, pp. 315–335. doi:10.1007/978-3-319-12886-3_15, URL <https://doi.org/10.1007/978-3-319-12886-3{15}>.
- [19] Uranga, A., Persson, P.-O., Drela, M., and Peraire, J., “Implicit large eddy simulation of transition to turbulence at low Reynolds numbers using a discontinuous Galerkin method,” *International Journal for Numerical Methods in Engineering*, Vol. 87, No. 1-5, 2011, pp. 232–261. doi:10.1002/nme.3036, URL <http://dx.doi.org/10.1002/nme.3036>.
- [20] de Wiart, C. C., and Hillewaert, K., “Development and validation of a massively parallel high-order solver for DNS and LES of industrial flows,” Springer International Publishing, Cham, 2015, pp. 251–292. doi:10.1007/978-3-319-12886-3_13, URL <https://doi.org/10.1007/978-3-319-12886-3{13}>.
- [21] Pazner, W., Franco, M., and Persson, P.-O., “High-order wall-resolved large eddy simulation of transonic buffet on the OAT15A airfoil,” *AIAA Scitech 2019 Forum*, AIAA SciTech Forum, American Institute of Aeronautics and Astronautics, 2019. doi:doi:10.2514/6.2019-1152, URL <https://doi.org/10.2514/6.2019-1152>.
- [22] Fernandez, P., Nguyen, N. C., and Peraire, J., “A physics-based shock capturing method for unsteady laminar and turbulent flows,” *56th AIAA Aerospace Sciences Meeting*, Orlando, Florida, 2018, pp. AIAA–2018–0062.
- [23] Moro, D., Nguyen, N. C., and Peraire, J., “Dilation-based shock capturing for high-order methods,” *International Journal for Numerical Methods in Fluids*, Vol. 82, No. 7, 2016, pp. 398–416. doi:10.1002/fld.4223.
- [24] Cockburn, B., and Shu, C.-W., “The local discontinuous Galerkin method for time-dependent convection-diffusion systems,” *SIAM Journal on Numerical Analysis*, Vol. 35, No. 6, 1998, pp. 2440–2463. doi:10.1137/S0036142997316712, URL <http://pubs.siam.org/doi/abs/10.1137/S0036142997316712>.
- [25] Nguyen, N. C., and Peraire, J., “Hybridizable discontinuous Galerkin methods for partial differential equations in continuum mechanics,” *Journal of Computational Physics*, Vol. 231, No. 18, 2012, pp. 5955–5988. doi:10.1016/j.jcp.2012.02.033, URL <http://linkinghub.elsevier.com/retrieve/pii/S0021999112001544>.
- [26] Alexander, R., “Diagonally implicit Runge-Kutta methods for stiff ODEs,” *SIAM J. Numer. Anal.*, Vol. 14, 1977, pp. 1006–1021.
- [27] Marquardt, D. W., “An algorithm for least-squares estimation of nonlinear parameters,” *SIAM*, Vol. 11, No. 2, 1963, pp. 431–441.

- [28] Grepl, M. a., Maday, Y., Nguyen, N. C., Patera, A. T., and C., N. N., “Efficient reduced-basis treatment of nonaffine and nonlinear partial differential equations,” *ESAIM: Mathematical Modelling and Numerical Analysis*, Vol. 41, No. 3, 2007, pp. 575–605. doi:10.1051/m2an:2007031, URL <http://www.esaim-m2an.org/10.1051/m2an:2007031>http://journals.cambridge.org/abstract_S0764583X07000313.
- [29] Rozza, G., Huynh, D. B. P., and Patera, A. T., “Reduced basis approximation and a posteriori error estimation for affinely parametrized elliptic coercive partial differential equations: Application to transport and continuum mechanics,” *Archives Computational Methods in Engineering*, Vol. 15, No. 4, 2008, pp. 229–275.
- [30] Nguyen, N. C., “A multiscale reduced-basis method for parametrized elliptic partial differential equations with multiple scales,” *J. Comput. Phys.*, Vol. 227, No. 23, 2008, pp. 9807–9822.
- [31] Broyden, C. G., “The convergence of a class of double-rank minimization algorithms 1. General considerations,” *IMA Journal of Applied Mathematics*, Vol. 6, No. 1, 1970, pp. 76–90. doi:10.1093/imamat/6.1.76, URL <http://imamat.oxfordjournals.org/content/6/1/76.abstract>.
- [32] Fletcher, R., “A new approach to variable metric algorithms,” *The Computer Journal*, Vol. 13, No. 3, 1970, pp. 317–322. doi:10.1093/comjnl/13.3.317, URL <http://comjnl.oxfordjournals.org/content/13/3/317.short?rss=1&ssource=mfc>.
- [33] Goldfarb, D., “A family of variable-metric methods derived by variational means,” *Mathematics of Computation*, Vol. 24, No. 109, 1970, pp. 23–23. doi:10.1090/S0025-5718-1970-0258249-6, URL <http://www.ams.org/mcom/1970-24-109/S0025-5718-1970-0258249-6/>.
- [34] Shanno, D. F., “Conditioning of quasi-Newton methods for function minimization,” *Mathematics of Computation*, Vol. 24, No. 111, 1970, pp. 647–647. doi:10.1090/S0025-5718-1970-0274029-X, URL <http://www.ams.org/mcom/1970-24-111/S0025-5718-1970-0274029-X/>.
- [35] Pazner, W., and Persson, P. O., “Approximate tensor-product preconditioners for very high order discontinuous Galerkin methods,” *Journal of Computational Physics*, Vol. 354, 2018, pp. 344–369. doi:10.1016/j.jcp.2017.10.030.
- [36] Cecka, C., Lew, A. J., and Darve, E., “Assembly of finite element methods on graphics processors,” *International Journal for Numerical Methods in Engineering*, Vol. 85, No. 5, 2011, pp. 640–669. doi:10.1002/nme.2989.
- [37] Geuzaine, C., and Remacle, J. F., “Gmsh: A 3-D finite element mesh generator with built-in pre- and post-processing facilities,” *International Journal for Numerical Methods in Engineering*, Vol. 79, No. 11, 2009, pp. 1309–1331. doi:10.1002/nme.2579.
- [38] Lee, B., “Oscillatory shock motion caused by transonic shock boundary-layer interaction,” *AIAA journal*, Vol. 28, No. 5, 1990, pp. 942–944.
- [39] Hartmann, A., Feldhusen, A., and Schröder, W., “On the interaction of shock waves and sound waves in transonic buffet flow,” *Physics of Fluids*, Vol. 25, No. 2, 2013, p. 026101.

- [40] Alshabu, A., and Olivier, H., “Unsteady wave phenomena on a supercritical airfoil,” *AIAA journal*, Vol. 46, No. 8, 2008, pp. 2066–2073.